

Structure and Host-Guest Interactions of Perylene-Diimide Dyes in Zeolite L Nanochannels

Lara Gigli^{1*}, Rossella Arletti^{2,3}, Gloria Tabacchi⁴, Marco Fabbiani⁴, Jenny G. Vitillo^{4,±}, Gianmario Martra^{3,5}, Andre Devaux⁶, Ivana Miletto⁷, Simona Quartieri⁸, Gion Calzaferri⁹ and Ettore Fois^{4*}.

¹ Elettra-Sincrotrone Trieste strada Statale 14 - km 163,5 in AREA Science Park
I-34149 Basovizza, Trieste, Italy

² Department of Earth Sciences, University of Torino, Via Valperga Caluso 35, I-10125-Torino, Italy.

³ Interdepartmental Center “Nanostructured Interfaces and Surfaces, University of Torino, Via P. Giuria 7, I-10125
Torino, Italy.

⁴ Department of Science and High Technology and INSTM, Università degli Studi dell’Insubria, Via Valleggio 11,
I-22100-Como, Italy

⁵ Department of Chemistry, University of Torino, Via Pietro Giuria 7, I-10125-Torino, Italy

⁶ PicoQuant GmbH, Rudower Chaussee 29, D-12489 Berlin, Germany

⁷ Department of Science and Technological Innovation, University of Eastern Piedmont, Viale Teresa Michel 11,
I-15100-Alessandria, Italy

⁸ Department of Mathematics, Computing, Physical and Earth Sciences, University of Messina, Viale Ferdinando
Stagno d’Alcontres 3, I-98166-Messina S. Agata, Italy

⁹ Department of Chemistry and Biochemistry, Bern University, Freiestrasse 3, CH-3012 Bern, Switzerland.

[±] present address: Dept. of Chemistry, Univ. Minnesota, 207 Pleasant St SE,
Minneapolis, MN 55455-0431, USA

Abstract

Confinement-driven self-assembly of dyes in nanomatrices is an effective route for the production of hybrid supramolecular structures of high technological relevance, among which the archetypal zeolite L-based systems are exploited in Förster Resonance Energy Transfer (FRET)-sensitized solar cells, luminescent solar concentrators, color-changing media, but also sensing in analytical chemistry, biology, and diagnostics. Despite this progress in applications, the organization of confined chromophores in zeolite L materials remains elusive. Herein, by integrating experiments with different time scale and radiation source (IR, XRPD, Total Scattering) with first-principles DFT modeling, we attained a microscopically detailed picture of a technologically important hybrid composite of Zeolite L with a perylene-diimide (also known as perylene-bisimide) dye at both hydrated and anhydrous conditions. The asymmetric positioning of the dye in the zeolite channel is determined by two factors: shape-volume constraints, and relative strength of competitive interactions among confined species. Our multi-technique experimental-theoretical approach thoroughly described the supramolecular chemistry of this hybrid material, identifying possible strategies to further enhance FRET efficiency and improve functionality. This work deepens the understanding of host-guest interactions in dye-Zeolite L composites, a key requirement to master the finely-tuned mechanisms governing supramolecular organization in confined nanospaces.

1. Introduction

The realization of hybrid supramolecular structures via confinement-driven self-assembly of photoactive species in ordered porous materials is a convenient route for the production of technologically relevant host-guest systems that could be exploited in diverse areas, ranging from solar energy transport to effect pigments.^{1–11} In this field, zeolites, and in particular zeolite L (ZL),¹² have played a seminal role^{13,14} as ideal host materials, and their successful use in the fabrication of hybrid systems^{15–19} has been a stimulus for the search of new scaffolds suitable for the obtainment of exploitable organized supramolecular structures.^{20–30} From inorganic zeolitic frameworks, including semiconducting chalcogenides²⁰ and aluminophosphates,^{23,31} to the fully-organic channels of *e.g.* bis-urea macrocycle crystals²⁴ up to the larger pore spaces and the additional possibilities offered by mesoporous silica/organosilica materials,^{25–27} layered materials such as hydroxides and clays,^{2,32–34} and metal organic frameworks / covalent organic frameworks (MOFs and COFs),^{11,28–30} a multitude of host matrices has been tested, leading to innumerable new exciting materials whose immense potential still remains to be explored.

Apparently, to convert these new generations of hybrids into useful applications, a long distance still needs to be walked, along which the know-how gathered on zeolite L composites may act as a trusted guide and source of inspiration. As a matter of fact, both synthesis and post-fabrication procedures of zeolite L have reached a high sophistication level, allowing, for example, to modify selectively either the ZL channel entrances with functional molecules traditionally called “stopcocks”^{35–38} or the external surface of the zeolite with suitable linkers.^{17,39} Such a selective functionalization of the interface region has enabled, for instance, ZL crystals to be assembled in highly organized functional monolayers,^{17,18,40–42} embedded in polymer matrices,⁴³ and even exploited in molecular-recognition events.⁴⁴ Based on these principles, an outstanding diversity of ZL-based functional materials has been realized, in which unique electro-optical properties are imparted by the macroscale extension of the regular organization of the chromophores inside the one-dimensional nanochannels of zeolite L.^{45–50} Significantly, the latter feature not only is at the origin of the functional properties of the hybrids, but it also allows to control remotely the material response by means of external stimulations, such as electric⁵¹ or magnetic fields,⁵⁰ or, more commonly, irradiation with visible light.^{4,5,37,52}

On the other hand, notwithstanding the successes of ZL-composites as components of useful devices, and the continuous progresses of advanced microscopy techniques^{53–56} needed for their functional characterization, the microscopic level knowledge of these materials is still in its infancy.

1
2
3 Unfortunately, most plagued by this lack of knowledge is the atomistic-level structure of these
4 systems, which is determined by the host-guest interactions governing the organization of the
5 chromophores. Such knowledge would be pivotal for improving the confinement-driven self-
6 assembly processes of supramolecular architectures of dyes, as well as for suggesting new and
7 better-performing hybrid composites.⁵⁷⁻⁶⁰

8
9
10 Being zeolites crystalline aluminosilicates, structural data could be typically obtained by
11 diffraction studies. In general, current knowledge on dimensionality, size and structure of zeolite
12 pores is mostly based on X-ray diffraction data, both on single crystal and on powdered materials.⁶¹
13 Nonetheless, in the literature, there are very few diffraction studies on hybrid zeolite-dye systems⁶²⁻
14 ⁶⁵ – which highlighted, moreover, some difficulties in unambiguously defining the atomic positions
15 of the organic guests.⁶⁵ This difficulty is mainly due to the very fact that the scattering power of the
16 aluminosilicate framework is much higher than that of the lighter atoms normally found in most
17 organic dyes.

18
19
20 Substantial improvement in determining structure, positioning and supramolecular
21 organization of light-atom species inside zeolites can be achieved by combining X-rays studies with
22 other techniques; for example, with infrared and Raman spectroscopies – which unraveled
23 important details of the organization of methylviologen in ZL,⁶³ - or with appropriate modeling
24 investigations – which already captured the supramolecular organization of very complex confined
25 architectures with atomistic precision otherwise inaccessible.^{65,66}

26
27
28 Due to the explosion in computing power of the last decade, structural investigations on
29 zeolite adducts based essentially on modeling/simulation studies - often aided by UV-Vis
30 spectroscopy experiments - have flourished in the recent past⁶⁷⁻⁸¹ so that an extensive literature is
31 available, including important reviews.⁸² Besides providing structural information on the bulk
32 material, simulations also allow to study phenomena taking place at the zeolite pore entrances,^{38,83}
33 which are of topic relevance in the self-assembly of dye-zeolite adducts. More in general, the
34 convergence of different methods of analysis, enhanced by theoretical modeling, is already
35 recognized as the strategy-of-choice to solve difficult structural and dynamical problems in a
36 diversity of scientific domains.⁸⁴⁻⁸⁷

37
38
39 Based on these premises, by revealing the structure of a technologically important hybrid
40 composite and the interplay of competitive, non-covalent, molecular forces at its origin, our work
41 aims to set a viable approach for the structural elucidation of dye-ZL functional materials.

42
43
44 The structure of the neutral dye tb-DXP [N,N-bis (4-tert-butyl-2,6-dimethylphenyl)-3,4,9,10-
45 perylenetetracarboxylic diimide] inside the one-dimensional nanochannels of ZL was the specific
46 object of our study. The dye belongs to the perylene-diimide (also known as perylene-bisimide)

1
2
3 family,⁸⁸ a class of compounds that has received considerable attention for its outstanding
4 photophysical properties. Additionally, perylene-diimide dyes are particularly attractive as
5 functional elements of dye-zeolite materials, because they can be easily organized in one-
6 dimensional supramolecular arrangements when encapsulated in ZL matrices.^{45,46,48,89}

7
8
9 In this work, we assembled tb-DXP-ZL composites with high dye loading in order to ensure a good
10 resolution of the diffraction experiments - a factor of crucial importance for structural elucidation,
11 especially in such a challenging case. While a high concentration of dye molecules can affect the
12 photophysical properties of the adduct - and emission especially, because of self-absorption
13 processes,^{4,46} - the selected loading should reasonably ensure a sufficiently long spacing between
14 adjacent dye molecules. Since, under these conditions, dye-dye interactions should have only minor
15 effects on the structure of the encapsulated tb-DXP molecules, our conclusions could be also
16 transferred to more dilute tb-DXP-ZL composites.
17
18
19
20
21

22 By considering both the hydrated and anhydrous forms of the ZL/tb-DXP composite, the
23 host-guest and guest-guest interactions have been investigated *via* a combined
24 experimental/theoretical approach. The analyses included destructive methods (thermogravimetric,
25 mass spectrometry and chemical attack), allowing for the determination of the actual stoichiometry
26 of the composite, as well as non-destructive approaches (radiation-based methods), aimed at the
27 determination of atomistic-level structure, interactions and electronic properties. Synchrotron
28 radiation (SR) source was adopted for the structural analyses of powder samples. IR sources were
29 used for investigating the effect of the host matrix on the vibrational properties of tb-DXP, also
30 adopting deuterated water to better probe the guest-guest interactions. UV-Vis radiation was used
31 for confirming the (already known) photophysical properties of the anhydrous and hydrated
32 composites. Such a battery of experimental methods was, ultimately, combined with theoretical
33 calculations. Herein, we will show that by integrating results obtained by X-ray Powder Diffraction
34 (to probe average positions), total scattering experiments (to probe average distances), and IR
35 spectroscopy (to probe interactions strength), with theoretical modeling, one could achieve a
36 detailed microscopic picture of the self-assembled tb-DXP/ZL composite.
37
38
39
40
41
42
43
44
45
46
47

48 **2. Experimental and materials**

49 *2.1 Zeolite L*

50
51
52 The potassium zeolite L material used for this study was purchased from Tosoh Corporation
53 (Japan). It is characterized by the stoichiometric formula $K_{8.46}(Al_{8.35}Si_{27.53})O_{72} \cdot 17.91H_2O$, LTL-
54 framework type,⁶¹ Si/Al ratio = 2.9, space group P6/mmm,^{12,90} and the following cell parameters:
55
56
57
58
59
60

$a=18.3795(4)$, $c=7.5281(2)$, $V= 2202.4(1)$.⁶⁵The potassium zeolite L channel system has a large circular 12-membered ring (12MR) opening with a size of 10.10 Å (7.4 Å taking into account a van der Waals radius of 1.35 Å for the oxygen) and smaller elliptical 8-ring (8MR) openings with a size of 1.9×5.5 Å, both running parallel to the c axis.^{12,90} The main channels are connected to the 8MR ones by non-planar boat-shaped 8 membered rings (Figure 1a,b).

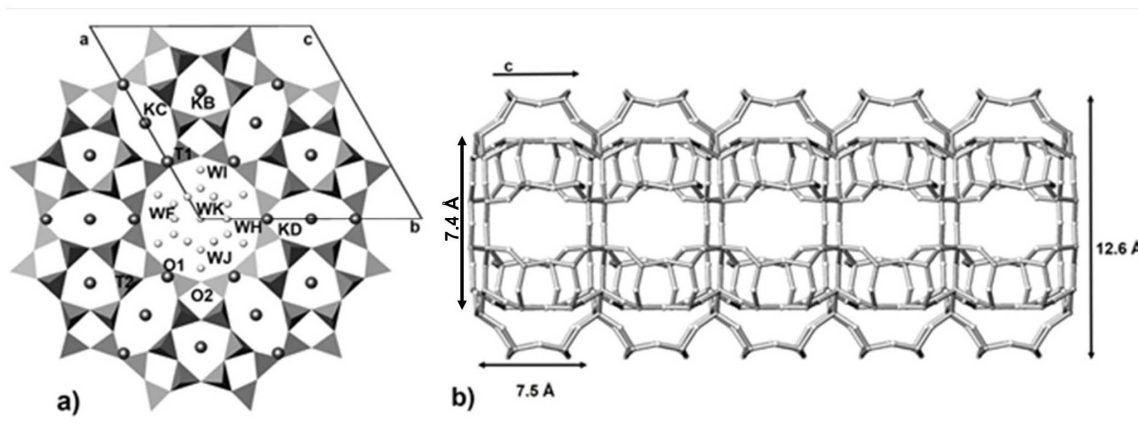


Figure 1. a) Projection of as-synthesized ZL structure along [001], showing the positions of relevant framework sites (T1, T2, O1, O2), water molecules (WF, WH, WI, WJ, WK) and potassium cations (KB, KC, KD). The exchangeable K^+ are those labelled KD. b) Projection of the ZL framework structure along [100] (that is, along the ZL channel).

2.2 Synthesis of *tb*-DXP dye and preparation of ZL/*tb*-DXP composites

The dye *tb*-DXP ($C_{48}H_{42}N_2O_4$, see Figure 2) was synthesized according to the procedure reported in Ref. ⁴⁶. It is a neutral molecule with dimensions of $6.75 \text{ \AA} \times 6.72 \text{ \AA} \times 26.16 \text{ \AA}$, when not considering the van der Waals radii. It presents a central flat perylene diimide core (consisting of five connected benzene rings), similar to other molecules belonging to the perylene family, with two 4-*tert*-butyl-2,6-dimethylphenyl functional end-groups. The size of these end-substituents, which determines the minimum core-to-core distance of adjacent dye molecules along the ZL channels, is large enough to prevent optical coupling typically found in aggregates.⁴⁵

The dye insertion was carried out through a gas phase procedure. In a typical experiment, 100 mg of ZL and 4.9 mg of *tb*-DXP⁴⁶ were weighed into a 25 mL round-bottom flask. Dichloromethane was then added, and the mixture was sonicated for 2 min to dissolve the dye and ensure a good dispersion of the zeolite. The solvent was then removed with the help of a rotary evaporator (40 °C, 600 mbar), thus leading to a homogeneous coating of the zeolite surface with *tb*-DXP. The coated zeolite was removed from the flask and transferred into an agate mortar, where it was ground up. The powder was then put into a small glass ampule and dried on a vacuum line for 24 h at a pressure of 2×10^{-2} mbar. The ampule was then sealed off under vacuum and put into a

rotating oven. The gas phase insertion process took place over 4 days at 260 °C. Once this process was completed, the ampule was removed from the heating source and cooled to room T. The ampule was then opened and the resulting pink powder was washed three times with 20 mL of dichloromethane until the supernatant was colorless.

In order to release the water from the zeolite channels without affecting the dye loading, the dehydration procedures were carried out at room T under vacuum for one night and then degassed at 200°C for two hours. A portion of the orange powder so obtained was then sealed in a 0.3 mm boron capillary for the diffraction measurements. For the spectroscopic analyses, the dehydration process was performed *in situ* in the measurement cells.

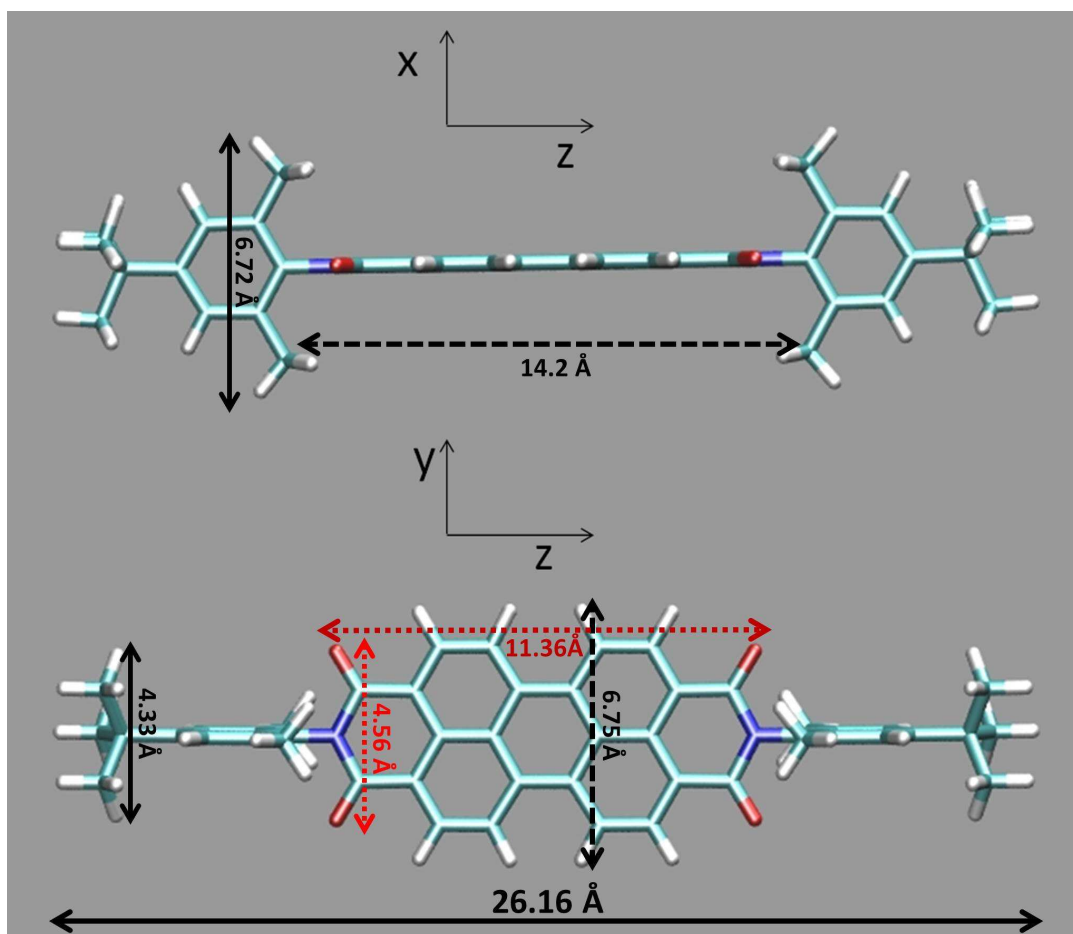


Figure 2. Calculated optimized structure of tb-DXP in the gas phase. Atom color code: C, cyan; O, red; N, blue; H, white. The z axis corresponds to direction along which the molecule is oriented in the ZL channel. Top panel: projection on the xz plane. Bottom panel, projection on the yz plane. The 2,6-dimethylphenyl groups are rotated by 90° with respect to the central perylene diimide core. The O-O separation is 11.36 Å along z, 4.56 Å along y. The separation of the 2,6-dimethylphenyl group along z is 14.2 Å. The dimensions of the molecule are: 26.16 Å along z (total length of the molecule), 6.72 Å along x (corresponding to the width of the 2,6-dimethylphenyl group) and 6.75 Å along y (corresponding to the lateral size of the perylene core). The width of the t-Bu groups is 4.33 Å. (See also supporting information, Table S3 and Figure S4)

2.3 HF Analysis

1
2
3 The loading level p of a dye-loaded zeolite is defined as the ratio of sites occupied by a dye to
4 the total number of sites in the sample. Thus, p in ZL sample can take values ranging from 0 (empty
5 ZL) to 1 (ZL fully loaded with dye). In this context, a site corresponds to the number (n_s) of ZL unit
6 cells required to host the full length of a single dye molecule. The value of n_s is usually given as an
7 integer number, but this is not a requirement.⁴
8
9

10 The loading level of the hydrated compound was determined by first suspending 2 mg of the
11 loaded material in 3 mL of distilled water in a polystyrene cuvette. 300 μ L of a 4% aqueous HF
12 solution were added to dissolve the zeolite. The ZL dissolution process was completed after 30 min;
13 at that time the aqueous phase was neutralized with a saturated solution of NaCO_3 and tb-DXP
14 molecules, which are insoluble in water, were extracted with dichloromethane. The concentration of
15 dye molecules in solution was calculated from the absorption spectrum and then the loading degree
16 was evaluated as a percentage of filled sites (p), by using three unit cells as the length of a site.^{45,46}
17
18
19
20
21
22
23

24 *2.4 TGA-MSEGA*

25 TGA-MSEGA analysis of as-synthesized ZL, pure tb-DXP and hydrated ZL/tb-DXP were
26 performed on a Seiko SSC 5200 thermal analyzer equipped with a quadrupole mass spectrometer
27 (ESS, GeneSys Quadstar 422) using the following experimental conditions: 10°C/min heating rate,
28 temperature range RT to 900 °C, air flux of 100 μ L/min. The gas phases emitted during the thermal
29 reactions were monitored in order to allow for the unambiguous identification of the species
30 responsible of the mass loss observed in the TGA curve. Gas analyses were carried out in Multiple
31 Ion Detection mode (MID), following the intensity of 8 species ($m/z = 16$ (CH_4), 18 (H_2O), 28
32 (CO), 30 (CH_3CH_3 , NO), 44 and 45 (CO_2), 78 (C_6H_6) and 76 (N_2O_3)) vs. temperature. Before
33 starting MID analysis, background subtraction was applied to set the zero point conditions. The
34 analysis was not performed on the dehydrated sample because, once exposed to air, it would have
35 retrieved water molecules.
36
37
38
39
40
41
42
43

44 *2.5 XRPD experiments*

45 X-Ray Powder Diffraction (XRPD) data of the hydrated ZL/tb-DXP composite were collected
46 at the SNBL (BM01a) beamline of ESRF (European Synchrotron Radiation Facility) – Grenoble
47 (France) in transmission geometry, with a fixed wavelength of 0.6825 Å. The powder sample was
48 loaded and packed in a 0.3 mm boron capillary, mounted on a standard goniometric head and
49 spun during data collection. The bi-dimensional diffraction pattern was recorded on a
50 PILATUS3 M-Series detector (pixel dimension 172 μ m) at a fixed distance of 193 mm from the
51 sample. The one-dimensional diffraction pattern was obtained in the 2θ range 0–50° by integrating
52
53
54
55
56
57
58
59
60

1
2
3 the two-dimensional image with the program FIT2D.⁹¹

4 The X-ray diffraction pattern of the dehydrated form of the hybrid system was collected at the
5 high resolution ID22 beamline of ESRF with a fixed wavelength of 0.4007 Å. The one-dimensional
6 diffraction pattern was obtained in the 2θ range 0–20°, combining nine high-resolution diffraction
7 patterns collected on nine Si (111) analyzer crystals.
8
9

10 Structural refinements were performed by full profile Rietveld analysis using the GSAS
11 package with the EXPGUI interface.⁹² The diffraction data did not reveal the presence of any
12 superstructure or symmetry change in the hydrated and dehydrated ZL/tb-DXP composites. Hence,
13 the refinements were performed in the parental ZL space group, P6/mmm. The atomic coordinates
14 reported by Gigli et al.⁶⁵ for the ZL framework atoms and the potassium cations were used as a
15 guess model. The other extraframework sites were derived by the inspection of the Fourier
16 difference maps (DELF). The Bragg peak profile was modeled using a pseudo-Voigt function with
17 0.01% cut-off peak intensity. The background curve was fitted using a Chebyshev polynomial with
18 23 variable coefficients. The 2θ-zero shift was accurately refined. The scale factor and the unit-cell
19 parameters were allowed to vary in all cycles. The refined thermal parameters for each data
20 histogram were assigned as following: the same thermal displacement value for all tetrahedral
21 atoms, a second value for all framework oxygen atoms, and a third one for the atoms of the tb-DXP
22 molecule. The thermal parameters of the potassium and the oxygen atoms of water molecules were
23 allowed to vary. Occupancy factors and isotropic thermal displacement factors were refined in
24 alternate refinement cycles.
25
26
27
28
29
30
31
32
33
34

35 Soft constraints were imposed on Si-O (1.63 Å), C–C (1.39-1.48 Å) and C-O (1.19-1.21 Å)
36 distances during the first stages of the refinements, and left free in the last cycles with tolerance
37 values of 0.03 Å.
38
39

40 The occupancy factors of the perylene diimide sites in both hydrated and dehydrated forms
41 were allowed to vary in the first refinement cycles and successively were fixed to an average value.
42

43 The final atomic positions, occupancy factors and thermal parameters of the hydrated and
44 anhydrous ZL/tb-DXP composites are given in Table S1. Table S2 reports the extraframework
45 interatomic distances.
46
47

48 The final observed and calculated powder patterns for the hydrated ZL/tb-DXP and anhydrous
49 ZL/tb-DXP composites are shown in Figure S1.
50
51

52 53 *2.6 Total scattering experiments*

54
55 These experiments were performed on the powder diffractometer of the ID22 beamline at the
56 synchrotron facility ESRF in Grenoble (France), using the Debye–Scherrer transmission setup (0.3
57
58
59
60

mm boron capillary), a monochromatic beam with a wavelength of 0.2066 Å (E = 60 keV) and an XRD 1611CP3 2D detector from Perkin Elmer at a distance of 399.4 mm. The selected photon energy combined with appropriate data collection (300 images with a counting time of 5 s) strategy enabled data acquisition over a sufficiently high wave vector Q ($Q=4\pi \sin\theta/\lambda$) to provide the necessary resolution in real-space for quantitative structural analysis to be attempted. Data were collected at room temperature up to $Q_{\max}=24.2\text{Å}^{-1}$ for empty ZL and tb-DXP-ZL composite. The experimental conditions were exactly the same for the two samples, which is of utmost importance to derive the differential pair distribution function (d-PDF). For each sample, images have been averaged and azimuthally integrated using the pyFAI software⁹³ to get the 2θ vs intensity pattern. The total scattering structure function S(Q) was obtained by normalizing the data to the incident flux and chemical composition of the samples. The experimental atomic pair distribution function G(r) in the real space was then obtained by a direct sine Fourier transformation of the resulting total scattering structure function S(Q), according to:

$$G(r) = \frac{2}{\pi} \int_{Q_{\min}}^{Q_{\max}} Q[S(Q) - 1] \sin(Qr) dQ$$

The scattering signal from the air and experimental setup (empty capillary) was measured independently under the exact same conditions as the sample and subtracted as a background in the data reduction procedure. In the Fourier transform step aimed to obtaining the experimental atomic pair distribution function G(r) from S(Q), the data were truncated at a finite maximum value of $Q_{\max}=22 \text{Å}^{-1}$ beyond which the signal-to-noise ratio became unfavorable. All data processing was done using the program pdfgetx3.⁹⁴

2.7 Spectroscopic methods

UV-Vis Absorption spectroscopy. Diffuse reflectance (DR) measurements in the visible range of the ZL/tb-DXP sample were performed on a Varian Cary 5000 spectrometer equipped with a reflectance sphere with the inner surface coated with Spectralon®. The spectra were acquired on loose powders diluted in polytetrafluoroethylene (PTFE, Teflon) and placed inside the standard powder cell of the instrument. The rationale of dilution was the attainment of an overall absorption intensity low enough to allow a correct use of the Kubelka-Munk function (KM) for the conversion of diffuse reflectance spectra. A composite/PTFE mass ratio of 1:22 resulted in reflectance (R) values in the $0.2 < R < 0.6$ range (i.e. $1.0 > KM > 0.13$) recommended as the most favorable one for the application of the KM function.⁹⁵

For the dehydrated ZL/tb-DXP composite, PTFE was previously outgassed overnight at 120°C before mixing with the sample in a glove box. For the acquisition in transmission mode (path length

1
2
3 10 mm) of the absorption spectrum of tb-DXP, a 10^{-7} M solution of the molecule in
4 dichloromethane was used.

5
6 *IR spectroscopy in transmission mode.* In situ IR spectra in transmission mode (2 cm^{-1} resolution,
7 average on 32 scans) were collected on a Bruker Vertex70 spectrophotometer. The samples were
8 measured in the form of self-supporting pellets inside a quartz cell equipped with KBr windows.
9 The cell was attached to a conventional vacuum line (residual pressure 1.0×10^{-5} mbar) allowing
10 thermal treatments and adsorption-desorption experiments to be carried out without re-exposing the
11 samples to ambient atmosphere. Deuterated water (99.9 atom %D) was supplied by Sigma Aldrich
12 and admitted onto the sample chamber after several freeze-pump-thaw cycles.

13
14 *IR spectroscopy in ATR mode.* IR spectra in air (2 cm^{-1} resolution, average on 256 scans) were
15 collected in Attenuated Total Reflection (ATR) mode on loose powder on a Bruker Vertex70
16 instrument (with a DTGS detector), equipped with a Bruker OPTIK Platinum ATR accessory
17 (internal reflection element in diamond). Atmospheric carbon dioxide and moisture signals were
18 subtracted by applying the Atmospheric Correction tools as implemented in the Opus 6.5 software.

26 27 2.8 Modeling

28
29 The framework was modeled using a simulation cell composed of four ZL crystallographic unit
30 cells along the channel axis, corresponding to the c crystallographic axis (or z axis). The framework,
31 whose stoichiometry was $[\text{Al}_{36}\text{Si}_{108}\text{O}_{288}]$, contained 36 potassium extraframework cations. The dry
32 model system contained one tb-DXP moiety (0.25 tb-DXP p.u.c.) (Figure 3a,b), while the hydrated
33 model system included also 24 H_2O molecules (Figure 3c,d). With such a stoichiometry, the
34 hydrated model contains 0.25 tb-DXP and 6 H_2O p.u.c. respectively (see Figure 3 for a graphical
35 representation of both models). The dimensions of the hexagonal simulation cells were obtained
36 from the experimentally detected ones (Table 2) by multiplying by 4 the c parameters, yielding thus
37 $a=18.4269\text{\AA}$; $c=30.0864\text{\AA}$ and $a=18.4262\text{\AA}$; $c=30.0844\text{\AA}$ for the dry and the hydrated model
38 system, respectively. The PBE approximation to Density Functional Theory was adopted for the
39 electronic interactions. Ultra-soft pseudopotentials were adopted to account for the nuclei-electrons
40 interactions. The tail-to-head interaction of the tb-DXP molecules were augmented with Grimme
41 DFT-D2 approximation in order to include long-range dispersion contributions; specifically, the
42 DFT-D2 corrections were applied to all atoms of the two 4-tert-butyl-2,6-dimethylphenyl groups of
43 tb-DXP. Electronic wave functions were expanded in planewaves (PW) basis set up to a kinetic
44 energy cutoff of 25 Ry (200 Ry for the electronic density representation). Such a computational set
45 up (designed as PBE/PW from now on) has been previously adopted for the study of host-guest
46
47
48
49
50
51
52
53
54
55
56
57
58
59
60

systems,^{96–100} adsorbate-surfaces interactions^{101–103} and also in the modeling of stopcock-functionalized ZL channel entrances.³⁸

Geometry optimizations were performed for both systems, adopting a quasi-Newton minimization scheme, with a maximum force of 5.0×10^{-4} hartree/bohr per atom as optimization criterion. Guess structures for geometry optimization were obtained via a series of Simulated Annealing processes via First-Principles Molecular Dynamics (FPMD),^{104,105} using the same approximations adopted for the geometry optimizations. Both FPMD runs and optimizations of the hydrated and dry systems were carried out using the CPMD code.^{104,105}

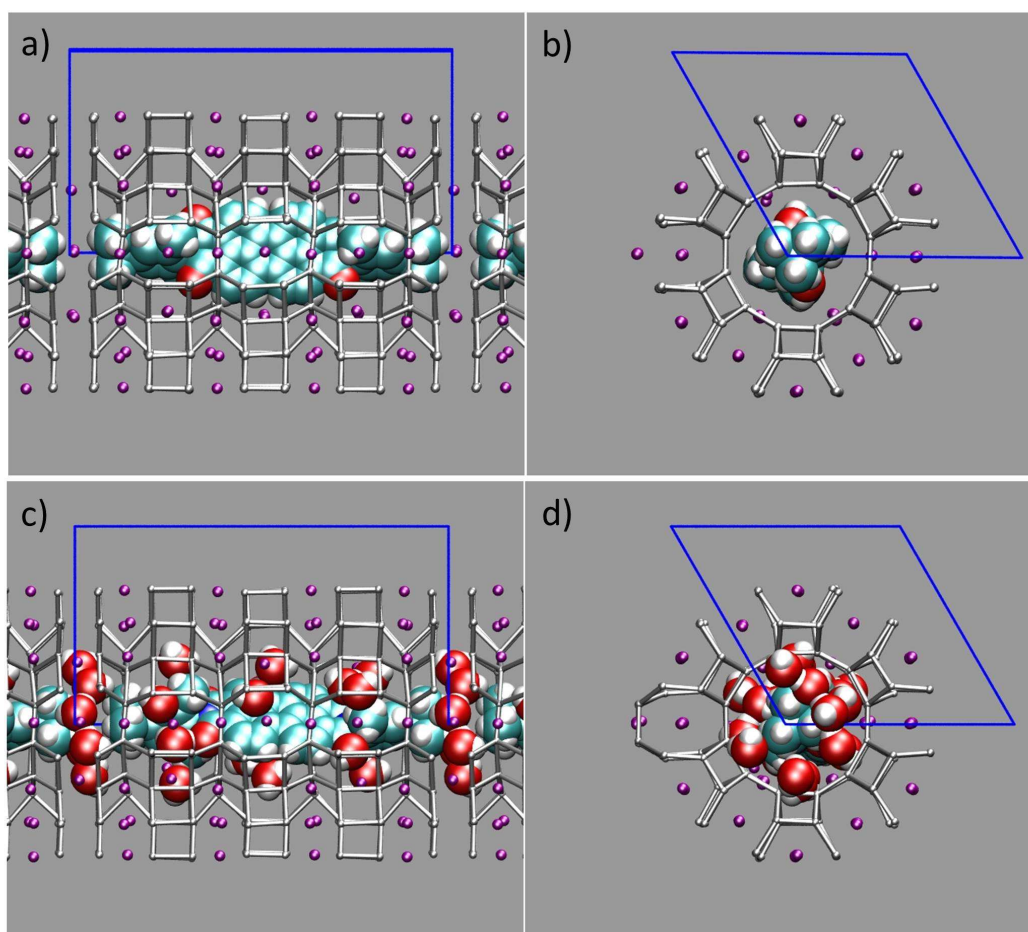


Figure 3. a)-b): Graphical representation of the minimum energy structure of the anhydrous tb-DXP/ZL system projected a) in the yz plane; b) in the xy plane. c)-d): Graphical representation of the minimum energy structure of the hydrated tb-DXP/ZL system projected a) in the yz plane; b) in the xy plane. In all panels (a),b),c),d): only the Al/Si atoms of the framework (gray sticks) are represented for clarity. The tb-DXP and water molecules are shown in van-der-Waals representation. Color codes: C=cyan; N=blue; O=red; H=white; K^+ =purple. The blue solid lines are a guide for the eyes and indicate the (periodically repeated) adopted simulation cell.

Cluster models were extracted from the minimum energy structures and used to calculate TD-DFT electronic excitations by adopting the hybrid functional CAM-B3LYP. The clusters contained the tb-DXP molecules and four K^+ cations, which were selected on the basis of their proximity to the

1
2
3 carbonyl oxygen atoms of tb-DXP. Each cation was surrounded by four point charges (-0.25e) in
4 order to keep electroneutrality. The positions of the point charges corresponded to those of the four
5 framework oxygen atoms closest to each selected potassium cation. In the case of the hydrated
6 model system, four water molecules were included in addition to the closest four potassium cations.
7 Calculations were performed using the basis set 6-311++g(d,p) for all atoms but K, for which
8 Stuttgart-Dresden ECP (SDD) pseudopotential and basis set were adopted. The data herein reported
9 for the geometrical parameters and vibrational normal modes of the isolated tb-DXP molecule have
10 been obtained by adopting the cc-pVTZ basis set and the B3LYP hybrid functional. Such a DFT
11 functional/basis set combination has been selected after performing (on the isolated tb-DXP
12 molecule) geometry optimization calculations at different levels of theory, which overall gave
13 comparable geometries (see Supporting Information, Table S3 and Figure S4). In order to aid
14 assignment of the experimental IR frequencies, besides the isolated tb-DXP, the harmonic
15 vibrational frequencies were calculated at the B3LYP/cc-pVDZ level of theory for two auxiliary
16 model systems: i) tb-DXP + H₂O, describing the interaction with a water molecule; ii) tb-DXP +
17 K⁺, describing the interaction with a potassium cation. For cluster and isolated molecule
18 calculations, the GAUSSIAN 09 code was used.¹⁰⁶

3. Results

3.1 TGA-MSEGA and HF analysis

31
32
33 Figure 3 shows the TG and DTG curves for the as-synthesized ZL and hydrated ZL/tb-DXP
34 composite compared with those of the pure crystalline tb-DXP. The derived values of molecules
35 hosted in the zeolite channels are listed in Table 1, where also the results of the HF analysis and
36 structural refinement (commented on in subsection 3.2) are reported. The water mass loss of the
37 hydrated composite (4.3 wt.%), occurring in the temperature range from 25 to 105°C, corresponds
38 to a total water content of 6.5 molecules per unit cell (p.u.c.). This number is lower than that
39 reported⁶⁵ for the as-synthesized ZL (Figure 4 and Table 1) consistently with the presence of the
40 tb-DXP molecules in the channels, that limits water re-adsorption after composite preparation.

41
42
43
44
45
46
47
48
49
50
51
52 The amount of dye loaded inside the hydrated ZL/tb-DXP system, evaluated on the basis of
the mass loss occurring in the range from 320 °C to 570 °C (5.8 wt.% in Figure 4), corresponds to
0.23 tb-DXP molecules p.u.c. (Table 1). This value is in good agreement with the loading of 0.17
molecules p.u.c provided by the HF analysis.

53
54
55
56
57
58
59
60 The tb-DXP release/decomposition from the composite occurs in one step in the same temperature
range from 320 °C to above 570 °C, where the decomposition of the solid dye also occurs.

Sample	Water loss T (°C)	Waterloss wt. %	Water molecules (TGA)	Water molecules (structure refinement)	tb-DXP loss T(°C)	tb-DXP loss wt.%	tb-DXP molecules p.u.c. (HF analysis)	tb-DXP molecules p.u.c. (TGA)	tb-DXP molecules p.u.c. (structure refinement)
ZL	110	11.9	18	18	-	-	-	-	-
ZL/tb-DXP	105	4.3	6.5	6.3	470	5.8	0.17	0.23	0.25

Table 1. Temperature values of water and tb-DXP mass losses and corresponding number of molecules, determined by TGA-MSEGA, compared to those obtained by the Rietveld refinement for the as-synthesized ZL and the hydrated ZL/tb-DXP composite.

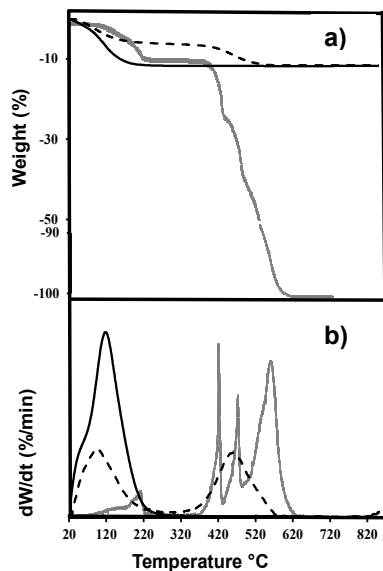


Figure 4. TG (a) and DTG curves (b) in air with a 10°C/min heating ramp for the as-synthesized ZL (black solid curve), solid tb-DXP (grey curve) and the hydrated composite ZL/tb-DXP (black dashed curve).

3.2 Structure refinements

Before presenting the structural features of the composite as obtained from the refinement (Table 2), we discuss the optimized geometry of the isolated guest molecule (Figure 2) and compare it with the dimensions of the confining environment – namely, the ZL nanochannels (see Figure 5).

Because the perylene core (Figure 2) is longer than the channel opening of ZL (~ 7 Å),^{12,65} the tb-DXP molecule can be encapsulated only with its longest molecular axis parallel to the one-dimensional ZL channel (see also Figure 3). This fact is at the origin of the functional properties of the composite: as the electronic transition dipole moment (ETDM) of tb-DXP is parallel to the long molecular axis, incorporation of tb-DXP in ZL nanochannels yields linear arrays of highly absorbing chromophores with parallel orientation of the ETDM, which guarantees an extremely high speed for FRET and therefore an extremely fast exciton transport.^{46,48,89}

A second important structural aspect is that tb-DXP can be considered composed by units of

quite different shape and size. The dye has a flat central perylene core 6.75 Å wide, symmetrically bound to two 2,6-dimethylphenyl residues (see Figure 2). Due to the presence of the methyl substituents, the 2,6-dimethylphenyl groups (6.72 Å wide), separated by ~14 Å from each other, are nearly orthogonal to the perylene-diimide plane (see Figure 2). The dye is terminated by two *tert*-butyl (t-Bu) groups, symmetrically linked to the two phenyl rings. The size of the t-Bu groups (4.33 Å, see Figure 2) is much smaller than the minimum diameter of the ZL channel, corresponding to the 12M-ring (see also Figure 3).

The above quoted lengths are atom-atom separations; however, by taking into account the van der Waals radii, the actual width of the dye is very close to the minimum diameter of the 12MR ring, which amounts to 7.4 Å considering van der Waals radii (see Table 3 and Figure 5). As in ZL the 12MR rings periodically alternate with a 7.5 Å spacing, and the maximum diameter of the channel amounts to 12.6 Å, the perylene core and the 2,6-dimethylphenyl groups should be reasonably localized in the largest sections of the ZL channels, irrespective of the presence of water.

Zeolite framework

The refinements of the unit cell parameters of hydrated and anhydrous ZL/tb-DXP composites provide similar values (Table 2).

Samples	ZL/tb-DXP hydrated	ZL/tb-DXP anhydrous
Space Group	P6/m m m	P6/m m m
a (Å)	18.4262(5)	18.4269(2)
c (Å)	7.5211(3)	7.5216(1)
V (Å³)	2211.4(1)	2211.8(1)
R_p (%)	3.6	7.2
R_{wp} (%)	5.0	9.7
R F² (%)	9.4	14.0
No. of variables	65	71
No. of observations	2227	9741
No. of reflections	948	397

Table 2. Experimental and refinement parameters for hydrated and anhydrous ZL/tb-DXP form.

With respect to the as-synthesized ZL, the structure undergoes some changes involving both the 12MR and 8MR channels running parallel to the *c* axis, particularly evident in the anhydrous form (see Table 3).

Sample ^a	12MR		8MR	
	O1-O1 ^b	O2-O2	O1-O1	O5-O5
ZL ^c	10.10	10.43	8.29	4.87
Hydrated ZL/tb-DXP	10.07	10.41	8.36	4.71
Anhydrous ZL/tb-DXP	9.43	10.30	8.99	4.62

Table 3. Diameters (in Å) of the 12MR and 8MR channels for ZL, hydrated ZL/tb-DXP and anhydrous ZL/tb-DXP.

^aExperimental values, obtained from the XRPD refinements.

^bAtom labels are defined in Figure 5.

^c From Ref.⁶⁵

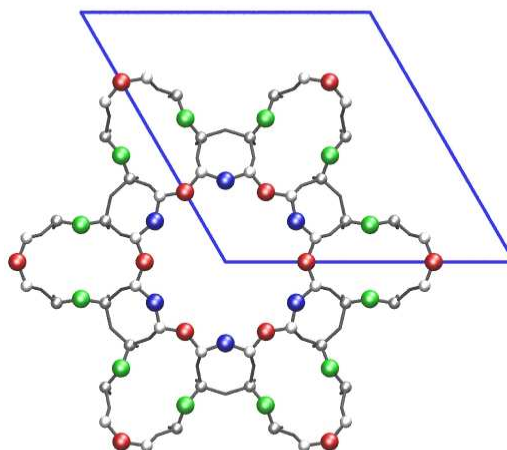


Figure 5. Graphical representation of the ZL framework structure projected in the xy plane, evidencing the 12MR and 8MR channels parallel to [001] and the hexagonal unit cell (solid blue lines). Atom color code: Si/Al=light grey; O1=red; O2=blue; O5=green. The other oxygen atoms of the framework are represented as gray sticks

The comparison of the normalized XRPD patterns collected on ZL and on the anhydrous and hydrated ZL/tb-DXP composites reveals slight differences in some peak intensities, particularly in the low 2θ region, which represents the part of the pattern most sensitive to the extraframework content and distribution. These changes in peak intensity ratios present in the composites are hints of the incorporation of tb-DXP into the channels, in agreement with the results of the TGA and HF analyses, which indicate the penetration of 0.23 and 0.17 molecules per unit cell, respectively.

The complex and highly symmetric structure of zeolite L and the low scattering power of the dye molecule atoms made localization of tb-DXP by XRPD a real challenge. Although the Fourier difference maps calculated for both composites showed many residual electronic density peaks, only the central perylene diimide core of the tb-DXP molecule was identified, and located close to the center of the channel. The other parts of the molecule were inferred by the results of the modeling and missing atoms were added in the refinement, conforming to the constraints imposed by the 6-fold symmetry of ZL structure. As above discussed, the 2,6-dimethylphenyl groups of the

1
2
3 end-substituents are bound to stay in a plane nearly perpendicular to the central flat core due to the
4 steric hindrance of the methyl groups in positions 2 and 6, while the external t-Bu groups might
5 rotate around the molecular axis.
6

7 *Water and dye molecules in the hydrated ZL/tb-DXP composite*

8
9 From the structure refinement of the hydrated ZL/tb-DXP pattern, 0.25 dye molecules were
10 found in the unit cell, in good agreement with TGA and HF results (Table 1). tb-DXP molecules are
11 sited at the center of the 12MR channel and lie on the mirror planes parallel to the *c* axis (See figure
12 S2). Due to the crystal symmetry, three different orientations of the molecule are possible.
13
14

15
16 Two independent, partially occupied water sites (WI and WX) were located in the 12MR
17 channel as well, accounting for a total of 6.3 molecules p.u.c., again in good agreement with TGA
18 data (Table 1). WI was also present in the starting structure of zeolite L, while WX is occupied only
19 in the composite (see Table S1 and S2, and Fig S2 a, b).
20
21

22 The distance K^+-O_{CO} , obtained from the structural refinement between the cationic KD sites
23 and the tb-DXP carbonyl oxygen sites, is 3.85 Å. Moreover, two water molecules (WI) are
24 coordinated to the K^+ cation at 2.89 Å and close to O_{CO} (see Table S2).
25
26

27 *Dye molecules in the anhydrous ZL/tb-DXP composite*

28
29 Also for this sample, the central perylene diimide core of tb-DXP was localized through the
30 differential Fourier maps. Six different orientations of the dye molecule are allowed. The molecule
31 is still sited at the center of the channel, but unlike in the hydrated form, only some atoms of the
32 molecule are sited on the mirror planes parallel to the *c* axis (Fig. S3), while the other ones have site
33 multiplicity of 24 because they are outside of the mirror planes parallel to the *c* axis. This makes the
34 refinement problematic due to the very low occupancy values of these sites (of the order of 0.02).
35 The structural experimental model suggests that the 2,6-dimethylphenyl groups of tb-DXP should
36 be perpendicular to the central perylene diimide core. Interestingly, such part of the molecule is
37 asymmetrically coordinated to the four closest KD sites, with two different distances, namely
38 $K^+-O_{CO}'=3.73\text{Å}$ and $K^+-O_{CO}''=3.55\text{Å}$.
39
40
41
42
43
44
45

46 *3.3 Total X-ray scattering results*

47
48 In the total scattering experiments, the interatomic distances involving the tb-DXP guest
49 molecules in the ZL cages were obtained by subtracting the contribution of a proper reference
50 sample – namely, hydrated ZL without dye loading.⁹⁵ In spite of the light-element composition of
51 tb-DXP (C, N, O and H) and the peak overlap, the differential pair distribution function (d-PDF,
52 obtained by subtracting the $G(r)$ of unloaded ZL from the $G(r)$ of loaded ZL) allowed to gain
53 important qualitative insight. Specifically, the d-PDF gave specific information on the distances
54
55
56
57
58
59
60

involving the tb-DXP dye, because the other distances present in both the tb-DXP loaded sample and the unloaded reference sample were subtracted out. Due to the impossibility to recreate *in situ* the preparation of the composite and then its dehydration, only the hydrated ZL/tb-DXP composite was investigated.

From the inspection of the d-PDF curve reported in Figure 6 it is possible to notice the following:

- i) the absence of sharp features beyond 5 Å, confirming that the encapsulation of the dye molecules did not perturb the structure of the zeolite matrix;
- ii) the bond distances in the tb-DXP molecule: 1.19 Å (C-O), 1.37 Å (C-C) and (C-N) – which are in good agreement with the values predicted by modeling (Table 4 and Table S3);
- iii) the interaction between the oxygen atoms of the dye carbonyl groups (O_{CO}) and the water molecules co-present in the structure, which contribute to the peaks at 1.84 Å ($O_{CO}-H_{water}$) and 2.85 Å ($O_{CO}-O_{water}$). Also these findings are well reproduced by modeling (Table 4).
- iv) the interatomic distances between K^+ ions and O_{CO} (2.85 Å, 3.44 Å, 4.35 Å, and 4.67 Å). Hence, four K^+-O_{CO} distances were deduced for the hydrated ZL/tb-DXP composite, while XRPD data indicated only one value (3.85 Å) This apparent contradiction was solved by computational results.

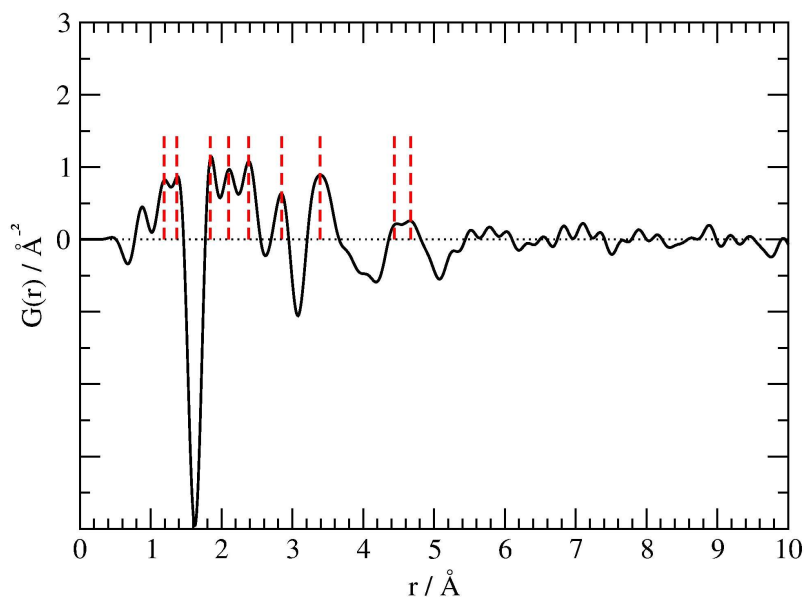


Figure 6. Differential PDF curve (ranging from 0 to 10 Å) obtained from subtracting the $G(r)$ of unloaded ZL from the $G(r)$ of loaded ZL. The main bonding features are traced by the red dashed line. The zero is represented as a dotted black line. The values relative to the carbonyl oxygen atoms are reported in table 4 and compared with the value obtained from the DFT calculations and the Rietveld refinement results. The peak at 1.37 Å corresponds to the C-C and C-N bonds, while the peaks at 2.10 Å and 2.38 Å are relative to next nearest C-H and C-C separations, respectively, in the tb-DXP molecule.

Table 4. Distances (in Å) relative to the carbonyl oxygen atoms of tb-DXP molecule from theoretical modeling, Rietveld refinement and d-PDF data of the hydrated system. Average values are highlighted in bold.

	Theory	Rietveld refinement	d-PDF
C-O_{co}	1.22	1.2	1.19
$\text{O}_{\text{co}}-\text{O}_{\text{H}_2\text{O}}$ (WX/WI)*	2.85	2.80/2.89	2.85
$\text{O}_{\text{co}}-\text{H}_{\text{H}_2\text{O}}$ (WX/WI)*	1.84/1.85/1.74 1.81 (average)	1.80/1.89**	1.84
K-O_{co}	3.06/3.35/4.40/4.56 3.84 (average)	3.85	2.85/3.44/4.35/4.67 3.82 (average)

* water molecules labeling in Figure S2

**distances were calculated taking in account a reasonable H-O bond distance in the water molecules of 1.0 Å.

3.4. Simulation results

The structure of the optimized tb-DXP/ZL dry adduct is shown in Figure 7a (see also Figure 3a,b). The perylene core is located in the larger-diameter region of the ZL channel. Because the intramolecular spacing between the 2,6 dimethyl-phenyl groups (14.2 Å, Figure 2) is rather close to twice the c parameter (~ 15 Å), these bulky groups are located in two non-adjacent ZL unit cells, and occupy the larger-diameter region of the channel (Figure 3a,b). The two 2,6 dimethyl-phenyl groups are oriented almost perpendicular to the nearly flat perylene core, which is aligned to one of the longest O2-O2 diameters of the 12MR ring (Figure 5).⁸³ Finally, the t-Bu groups are located close to the smallest regions of the channel (the 12MR ring).

In view of the gas phase tb-DXP C_s symmetry, one might in principle hypothesize that the most favorable arrangement should be the one with the perylene core just in the middle of one cage, and the two end groups symmetrically occupying the two adjacent cells. However, the minimum energy structure of the anhydrous adduct has a certain degree of asymmetry, as also detected by XRPD. Indeed, although K^+ cations could interact strongly with the four carbonyl oxygen atoms of the diimide core ($\text{K}^+\cdots\text{O}_{\text{CO}}$ interaction = 26 kcal/mol for perylene diimide⁸³), the separation between such oxygen atoms (~ 11.4 Å, Figure 2) is not commensurate with the separation between K^+ in two adjacent ZL cells (~ 15 Å).⁸³ Hence, the asymmetry is likely induced by the fact that the molecule cannot be coordinated with four K^+ simultaneously. In particular, the calculated minimum energy structure features a short $\text{K}^+\cdots\text{O}_{\text{CO}}$ distance, 2.940 Å, and three longer distances, namely 3.458 Å,

3.693 Å and 3.922 Å.

The optimized structure of the hydrated tb-DXP/ZL adduct (Figure 7b) indicates that the perylene core is aligned with the O2-O2 diameter, the two nearly perpendicular 2,6-dimethylphenyl groups are asymmetrically positioned in large-diameter region of the ZL channels, and the t-Bu groups are located close to the 12MR ring. Despite these similarities with the anhydrous adduct, the additional 24 water molecules actually do affect the tb-DXP arrangement in ZL: for example, the perylene plane is distorted with respect to the nearly flat structure found in the dry model. Most of the water molecules are located in the ZL channel region partially occupied by t-Bu atoms (Figure 3c,d and 7b). These molecules can be considered as typical “zeolitic” water,^{107–115} hence coordinated to the extraframework cations and involved in a complex network of hydrogen bond interactions with water and framework oxygen atoms.^{116–125} Other water molecules are positioned either upside or below the perylene plane. These molecules interact with K⁺ ions, are engaged in hydrogen bonding with both water and framework oxygens, and may also interact with the π -electron density of the perylene core.

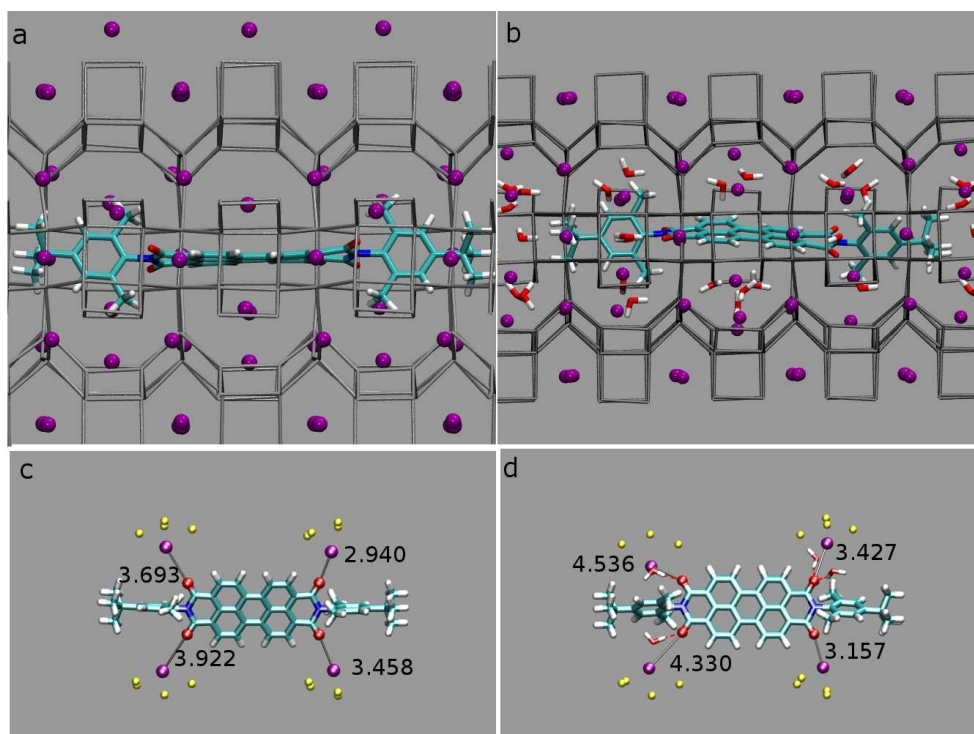


Figure 7. Panel a): Graphical representation of the minimum energy structure of the anhydrous tb-DXP/ZL system. Only the Al/Si atoms of the framework (gray sticks) are represented for clarity. C atoms are represented in cyan, N atoms in blue, oxygen atoms in red and hydrogen in white. The K⁺ cations are represented as purple spheres. Panel b): representation of the optimized structure for the hydrated tb-DXP/ZL adduct. Panel c): graphical representation of the tb-DXP molecule extracted from the optimized anhydrous system, along with the four closest potassium cations. Panel d): graphical representation of the tb-DXP molecule extracted from the optimized hydrated system. Also shown are the four closest K⁺ cations and the water molecules hydrogen bonded (red dashed lines) to the carbonyl oxygen atoms. In panel c) and d) the framework oxygen atoms (yellow spheres) close to the potassium cations are shown as well. In Panel c) and d) the four shortest K⁺···O_{CO} (in Å) are reported.

1
2
3 The most relevant group of water molecules is located close to the imide groups. In such a
4 region, many different interactions are competing. Zeolitic water has a strong affinity for the charge
5 compensating cations,^{126–129} and in the ZL/tb-DXP composite, there are 4 K⁺ *per* zeolite L unit cell
6 (corresponding to the crystallographic sites KD). Furthermore, several potential hydrogen bonding
7 partners are available: the framework oxygen atoms, the tb-DXP carbonyl groups, and other water
8 molecules. Also the carbonyl oxygen has a strong affinity for K⁺, and this is the strongest single
9 intermolecular interaction in this system.^{57,83} Nevertheless, as discussed previously and in ref.⁸³, the
10 perylene core cannot coordinate four K⁺ simultaneously.

11
12
13
14
15
16 Figure 7c,d represent the environment of the tb-DXP carbonyl oxygens in the anhydrous
17 (Fig 7c) and in the hydrated (Fig. 7d) system. In both cases, the geometry of the supramolecular
18 aggregate should be dominated by the K⁺⋯O_{CO} interactions, but the achievement of the most
19 favorable organization is hampered by distance mismatch. In the hydrated composite (Figure 7d)
20 only one carbonyl oxygen is interacting with K⁺ without the intermediation of water, and such a
21 contact is the shortest one, 3.157 Å. The other three carbonyl oxygens are hydrogen bonded to one
22 water in two cases – leading to K⁺⋯O_{CO} distances of 4.536 Å and 4.330 Å, and two water
23 molecules in the third case (K⁺⋯O_{CO} distance: 3.427 Å); such water molecules are in turn
24 coordinated to the potassium cations. Therefore, in agreement with the structural data (Table 4), the
25 main structural effect of water molecules is to increase the K⁺⋯O_{CO} distances, as previously
26 observed for other ZL-composites with carbonyl dyes.^{57,58,65} Both XRPD data and modeling
27 indicated water molecules close to both K⁺ and O_{CO}, hence a complex network of intermolecular
28 interactions, among which hydrogen bonds (typically below ~5 kcal/mol) are the weakest ones and
29 lie within the reach of thermal excitation energies at room temperature. Such hydrogen bonds may
30 easily break, causing a reorganization of the intermolecular interactions network inside the zeolite,
31 and specifically of the bonding partners of the perylene carbonyl groups. Hence, the XRPD finding
32 of four equivalent K⁺⋯O_{CO} distances (3.85Å, Table 4) can be understood by noting that the
33 timescales of such reorganization processes are much shorter than those typical of XRPD
34 measurement, and that those experiments provide average atomic *positions*. This interpretation is
35 supported by the Total Scattering data – which provide interatomic *distances* and are closer to the
36 modeling results.

37
38
39
40
41
42
43
44
45
46
47
48
49
50 Because the modeling of the hydrated ZL/tb-DXP system indicated that several water
51 molecules are at close distance from the perylene core, the guest/co-guest interaction was further
52 investigated by IR and visible absorption spectroscopies.

53 54 55 56 3.5 IR spectroscopy

Figure 8 shows the IR spectra of solid tb-DXP (curve a), dry ZL/tb-DXP (curve b) and hydrated ZL/tb-DXP (curve c) in the range from 1800 to 1250 cm^{-1} range, where bands mainly due to the C=O groups,¹³⁰ the central perylene diimide core (labeled as P) as well as tert-butyl and dimethylphenyl moieties (labelled as R) are present. As reported in the Experimental section, the low-frequency limit was determined by the onset of the most intense absorption from the zeolite lattice modes.

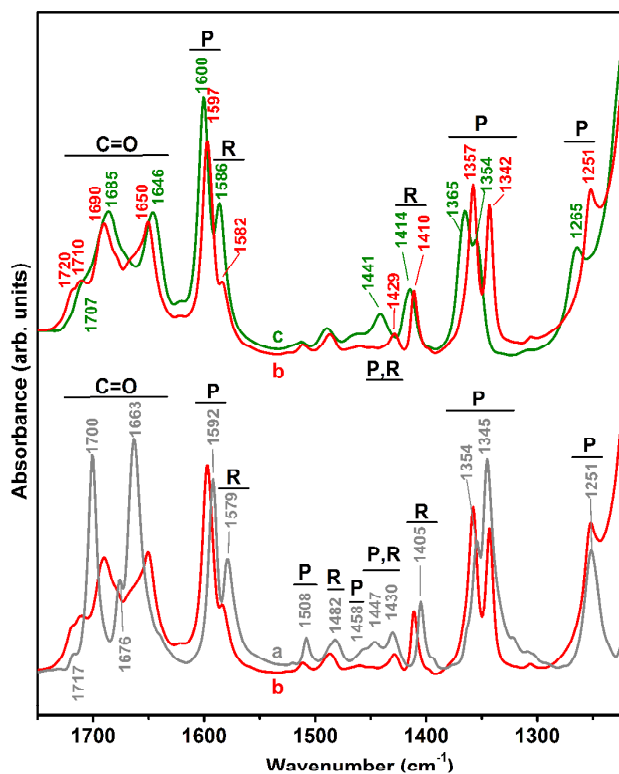


Figure 8. IR spectra, in the range of 1800 to 1220 cm^{-1} of: a) solid tb-DXP (gray curve); b) ZL/tb-DXP dried by outgassing at 200 $^{\circ}\text{C}$ for 1 h (red curve); c) ZL/tb-DXP subsequently hydrated by contact at RT with D_2O at 20 mbar (green curve). Spectrum b) is shown in both the lower and upper panel for the sake of comparison. Spectrum a) was obtained in the ATR mode, while spectra b) and c) in transmission in controlled atmosphere (see Experimental).

The basis for band assignment was provided by the calculated normal modes. As known, for large molecules such calculations provide a very large amount of data, resulting in a difficult interpretation with respect to the experimental vibrational spectrum. In the present case, this problem was addressed by calculating the normal modes of a tb-DXP molecule in vacuum and in interaction with a K^+ ion, or a H_2O molecule, thus selecting normal modes exhibiting a dependence on the interactions with the cation or water more similar to the behavior observed for experimental IR bands. The results are listed in Table 5, compiled using the experimental frequencies obtained for solid tb-DXP.

For solid tb-DXP (curve a), the $\nu\text{C=O}$ pattern is composed by two main peaks at 1700 and 1663 cm^{-1} , with weaker partners at 1717 and 1676 cm^{-1} , in agreement with the calculated four normal modes dominated by the C=O stretching displacements. When tb-DXP is embedded in the dried zeolite channels (curve b), all signals are split into unresolved components, with most of them downshifted by about 10-20 cm^{-1} . The interaction with K^+ ions can well account for the latter feature, whilst the increase in the signal multiplicity indicates that this interaction does not involve all carbonyl groups to the same extent.

Table 5. Assignment of the IR bands in Figure 8. The positions are those of the signals in the spectrum of solid tb-DXP (curve a).

position (cm^{-1})	Assignment, in terms of localization of normal modes (shown in the indicated figures of SI)	Figure(s) of the label in Figure 8 normal mode in the SI	
1717, 1700, 1676, 1663	4 normal modes with a significant C=O stretching amplitude	Fig. S5-S8	C=O
1592	breathing of the perylene diimide core	Fig. S9	P
1579	breathing of the aromatic ring of the 2,6 dimethylphenyl groups	Fig. S10	R
1508	other breathing of the perylene diimide core	Fig. S11	P
1482	other breathing of the aromatic ring of the 2,6 dimethylphenyl groups, with a significant localization also on C-N bonds	Fig. S12	R
1458	other breathing of the perylene diimide	Fig. S13	P
1450-1420	breathing of the perylene diimide core, combined with bendings of methyl groups	Fig. S14	P,R
1405	breathing of the aromatic ring of the 2,6 dimethylphenyl groups, combined with bendings of methyl groups	Fig. S15	R
1354	other breathing of the perylene diimide core, with a significant localization also on C-N bonds	Fig. S16	P
1345	similar to the previous one, with the additional bending, with small amplitude, of methyl groups	Fig. S17	P
1251	in plane bending of C-H in position 1,6,7,12 on the perylene diimide core	Fig. S18	P

At lower frequency, the bands due to the other structural elements of tb-DXP appear to be less sensitive to the change in environment resulting from the interaction with the zeolite host, in an anhydrous regime. In fact, the observed shifts are smaller, 5 cm^{-1} at maximum, and in the case of the peak at 1251 cm^{-1} - a band ascribed to a normal mode dominated by the in plane bending of C-H in 1,6,7,12 positions of the perylene core – its position is unshifted.

Conversely, the introduction of deuterated water molecules (in order to avoid interference with the $\delta\text{H}_2\text{O}$ mode at 1640 cm^{-1} , see Figure S19 in the SI) affected some of P (modes largely ascribable to the perylene core) and R bands (associated to the dimethylphenyl groups) in a larger effect than the

other components of the IR pattern (curve c). The $\nu\text{C}=\text{O}$ bands, the components in the 1620 to 1450 cm^{-1} range and the signal at 1410 cm^{-1} change position by a few wavenumbers, whereas a larger shift of 10-15 cm^{-1} occurs for signals at 1429 cm^{-1} , in the 1360 to 1340 cm^{-1} range, and at 1251 cm^{-1} .

Moreover, the inspection of the $\nu\text{D}_2\text{O}$ region provided also evidence for the effect of guest/co-guest/host interactions on water molecules (Figure 9), by comparing data obtained for the hydrated ZL/tb-DXP system (bottom panel) with a hydrated ZL (upper panel).

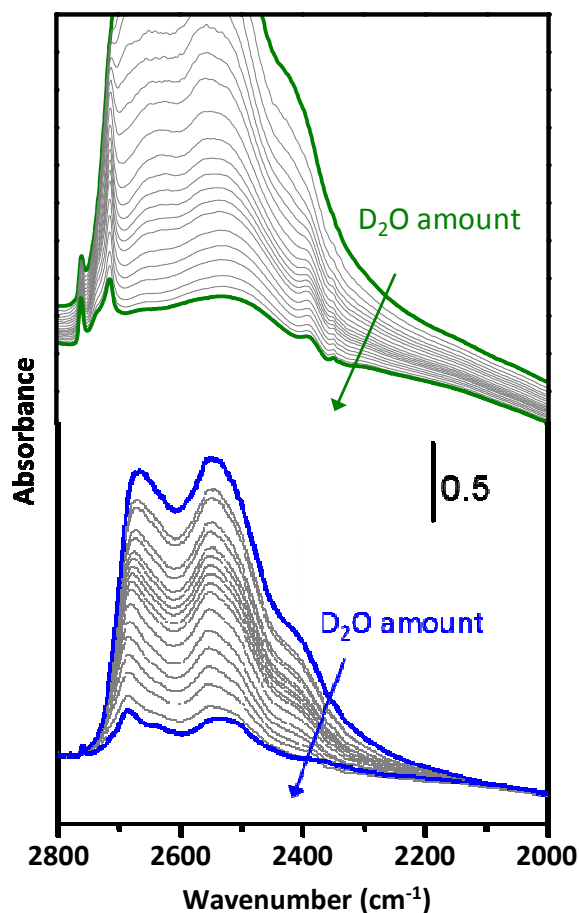


Figure 9 IR spectra in the range from 2800 to 2000 cm^{-1} of ZL (upper panel) and ZL/tb-DXP (lower panel) in contact at room T with D_2O at 20 mbar and then progressively outgassed. All spectra were collected in transmission mode under controlled atmosphere (see Experimental).

In the latter case, the amount of water molecules p.u.c in the fully hydrated samples was so high (see Table 1) as to result in a saturation of the $\nu\text{D}_2\text{O}$ signal. A series of spectra with decreasing $\nu\text{D}_2\text{O}$ signal intensity was then obtained by progressively outgassing, showing broad, overlapping components in the 2700 to 2200 cm^{-1} range, with a very weak narrow signal in the high frequency end due to deuterated hydroxy groups in defect positions. In the presence of tb-DXP, the amount of

1
2
3 water molecules that can be co-hosted in the zeolite channels decreases by ca. 2/3 (see Table 1), and
4 then the $\nu\text{D}_2\text{O}$ signals are no longer in saturation even at the highest possible hydration level. The
5 pattern recorded under this condition presents two main peaks at 2670 and 2545 cm^{-1} , both
6 asymmetric towards the high frequency side, and a shoulder component at 2415 cm^{-1} . The overall
7 spectral shape is maintained while decreasing the water content, with a progressively better
8 resolution for the series of sub-bands contributing to the two main signals. The difference with
9 respect to the previous case indicates that the state of water molecules is significantly affected by
10 the confinement between the zeolite host and tb-DXP guest: the signal sharpening and appearance
11 of sub-bands reflect both the occurrence of changes in the H(D)-bond networking and the limited
12 mobility of water molecules, likely experiencing a different local environment depending of their
13 location. In particular, the component initially located at 2670 cm^{-1} progressively up-shifts and
14 narrows when the amount of water decreases and seems to have no equivalent in the spectra of
15 water molecules in ZL. Both position and width of this signal suggest that it might be due to
16 “dangling”, non D-bonded OD moieties.¹³¹
17
18
19
20
21
22
23
24
25
26

27 3.6. UV-Vis absorption spectroscopy

28 DR UV-Vis spectra of anhydrous and hydrated ZL/tb-DXP composites, as well as of the dye in
29 CH_2Cl_2 solution, are reported in Figure 10. The spectrum of the dye in this last form in solution
30 displays a vibronic progression with main bands located at 525, 489, and 458 nm (curve a), which
31 appear almost unaffected in position when the environment is changed from dichloromethane to the
32 zeolite in the dry composite (curve b). Conversely, a bathochromic shift of 10-12 nm occurs as a
33 consequence of the hydration (curve c). A change in the electronic absorption when passing from
34 the anhydrous to the hydrated form was previously observed also for ZL/DXP composites,⁴⁵ and
35 ascribed to the formation of J aggregates. However, in the ZL/tb-DXP composite this aggregation is
36 prevented by the presence of tert-butyl substituents at both extremities of dye molecules. Thus, the
37 observed effect on the HOMO-LUMO energetic distance should result from the guest/co-guest/host
38 interaction. A confirmation was provided by the calculated electronic absorption intensities of the
39 two models depicted in Figures 7c and 7d, resulting in a bathochromic shift of the spectrum¹³² when
40 passing from the anhydrous to the hydrated composite (Figure 10a). For the sake of completeness, it
41 is reported that the high dye loading of the ZL/tb-DXP composite, which was mandatory for the
42 diffraction studies, falls in the loading range where severe inter particle self-absorption of
43 photoemission of DXP-based molecules occurs,⁴⁵ as assessed by photoluminescence measurements
44 of the composite (Figure S20 of the SI).
45
46
47
48
49
50
51
52
53
54
55
56
57
58
59
60

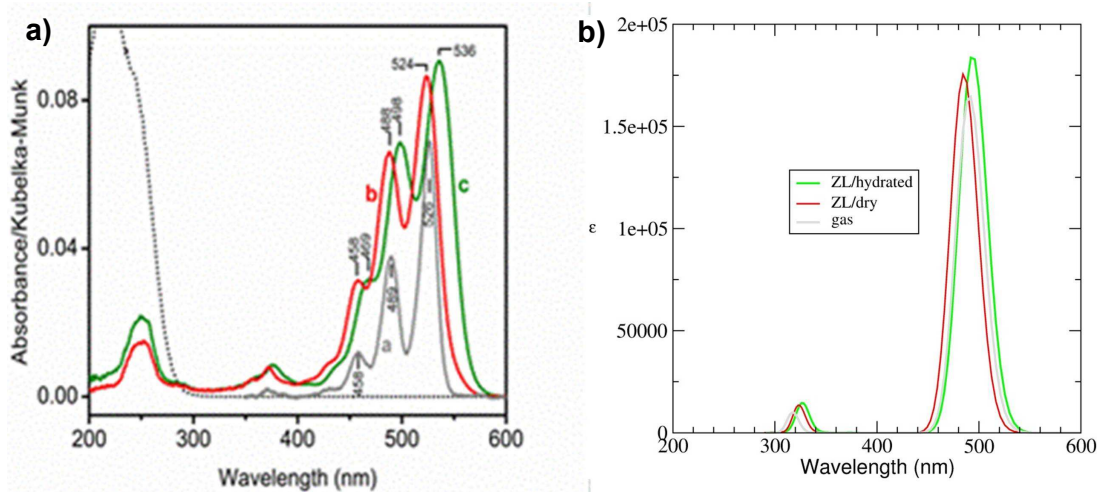


Figure 10. Panel a): DR UV-Vis spectra of the zeolite host (black dotted curve) and of: a) tb-DXP solution in dichloromethane (grey line); b) anhydrous ZL/tb-DXP (red line); c) hydrated ZL/tb-DXP (green line). Panel b): calculated electronic excitation intensities for anhydrous ZL/tb-DXP (red line), hydrated ZL/tb-DXP (green line) and isolated (vacuum) tb-DXP (grey line).

4. Discussion

Taken together, the presented data indicate that the host-guest interactions responsible for the self-assembled structure are determined by two main kinds of contribution: the first (and leading) one is due to shape-volume constraints, while the second is related to the relative strength of the interactions involving tb-DXP, potassium cations, water molecules and ZL framework.

The shape-volume constraints imply that: i) the tb-DXP molecule can be encapsulated only with its longest molecular axis parallel to the one-dimensional ZL channel; ii) the bulkier parts of the molecule occupy the wider parts of the ZL channel; iii) the four carbonyl groups cannot bind simultaneously four extraframework cations of ZL. Irrespective of the adopted technique, all of our data converge on this “coarse-grained” structural description. Such a picture is substantially unaffected by the absence/presence of water.

By focusing on finer details, in the refined structure the four, symmetrically arranged, oxygen atoms of the perylene carbonyl groups are on average separated from the closest K^+ cations by 3.65\AA in the anhydrous composite and 3.85\AA in the hydrated one. Such distances were obtained from average positions resulting from XRDP experiments on the time scales of minutes. Moreover, the (mobile) water molecules are competing with carbonyl oxygens to gain a stabilizing position close to the potassium cations. The carbonyl oxygens are more constrained than water oxygens because they belong to the quite rigid perylene core, whose translational degrees of freedom are limited by the shape-volume effects discussed above. Changes in the $K^+\cdots O_{CO}$ interactions due to hydration have been detected by monitoring the vibrational signals of the C=O groups on the much shorter

1
2
3 time scale of the IR spectroscopy. The water-induced modifications of the IR profiles are not
4 uniformly distributed over the C=O stretching region, indicating that on such short timescales the
5 four carbonyls are not symmetrically positioned with respect to the potassium cations. Such an
6 asymmetry is also detected by the Total Scattering experiments and supported by the modeling
7 studies. Instead, according to the XRPD analyses, whereas the anhydrous adduct was slightly
8 asymmetric, the hydrated composite showed a symmetric structure with four equivalent $K^+ \cdots O_{CO}$
9 distances. Indeed, while XRPD experiments provide uncorrelated average positions, Total
10 Scattering analyses focus on correlated interatomic distances,¹³³ and this difference is particularly
11 relevant when dealing with non-covalent non-ionic intermolecular interactions – as in the case of
12 hydrated ZL/tb-DXP. In the absence of water, the $K^+ \cdots O_{CO}$ interactions are maximized because
13 they have to compete solely with the rigidity of the molecule and the shape-volume constraints
14 imposed by the zeolite channel (both implying very strong energy penalty). Accordingly, both
15 XRPD and modeling indicate shorter $K^+ \cdots O_{CO}$ distances, and that the two shortest distances involve
16 oxygen atoms of the same imide group (Figure 7c). In the hydrated adduct, the greater $K^+ \cdots O_{CO}$
17 separation implies weaker interactions between K^+ and the carbonyl oxygens, which could cause,
18 on long timescales, the averaging of the four $K^+ \cdots O_{CO}$ distances as detected by XRPD. The
19 microscopic origins of the fast rearrangements of the hydrogen bond patterns, which affect the
20 $K^+ \cdots O_{CO}$ interactions, should be: i) the strained arrangement of the dye – which exhibits
21 appreciable out-of-plane distortions of the perylene core -, ii) the distance mismatch – which
22 prevents the simultaneous binding of the four carbonyl groups to potassium cations, and iii) the
23 presence of many competing interactions.

24
25
26
27
28
29
30
31
32
33
34
35
36
37 Previous studies of dye-ZL composites with smaller cationic dyes such as oxonine,⁵⁹
38 pyronine⁵⁹ and methylacridine,⁶⁰ revealed a major structural role of water in the
39 orientation/positioning of the confined dye: for example, in oxonine-ZL, water molecules may
40 switch the orientation of the chromophore with respect to the channel axis from parallel to
41 perpendicular.⁵⁹ Instead, in the composite formed by ZL and fluorenone,^{57,58,65} - another dye
42 containing a carbonyl group -, the effect of water was smaller: hydration led only to a modest
43 increase of the distance between the carbonyl oxygen and the potassium cation, because the
44 $K^+ \cdots O_{CO}$ coordination was by far the leading interaction. Therefore, water affects the
45 supramolecular organization of dye/ZL composites according to both shape-volume constraints and
46 relative strength of competing intermolecular interactions.

47
48
49
50
51
52
53 As mentioned in the introduction, the range of applications of zeolite L-dye composites is
54 impressive. Indeed, they offer a unique potential for developing FRET-sensitized solar cells,
55 luminescent solar concentrators (LSC), color-changing media, but also for sensing in analytical
56
57
58
59
60

1
2
3 chemistry, biology, and diagnostics, as extensively discussed in the literature.^{1,2,4,5,7,18,50,51,66}
4 Although it is not possible to claim that the tb-DXP/ZL composite represents the “best possible
5 combination” of host and guest - because it would mean that all possible combinations and their
6 properties with respect to all possible applications are known in detail - we can surely conclude that
7 the dye tb-DXP is an excellent guest for the fabrication of dye-ZL composites:
8
9

10 - because of its spectroscopic properties (range of the electronic absorption spectrum, high
11 fluorescence quantum yield, excellent spectral overlap that guarantees a very high FRET rate);
12
13

14 - because of its excellent structural properties that allow to realize a high loading of the
15 channels, ensuring at the same time sufficient separation between the chromophore-parts of the
16 molecules (because of the tb-groups, that work as spacers) so that J-coupling (which could result in
17 the creation of traps) is avoided^{45,89};
18
19

20 - because of its high chemical and photochemical stability;

21 - because of its carbonyl groups, which further improve the stability of the dye-ZL
22 composites (as demonstrated in earlier studies^{57,58,65,83}) and allow therefore to achieve a high
23 loading under moderate synthesis conditions.
24
25
26

27 Zeolite L bears some unique features, which make it currently the best possible choice as a
28 host for such hybrid composites. Its size and morphology can be tuned in a way not yet known for
29 any other host with one-dimensional channels; see e.g. ref.¹³⁴. The diameter of the channels
30 guarantees a high degree of ordering of the guests and allows to fine-tuning their interactions.^{1,89}
31 The composition of ZL has allowed developing the “stopcock principle”^{35,36,38,135} which makes use
32 of the specific chemical properties of the channel end, and has been unraveled in its atomistic
33 details by first-principles calculations.³⁸ Stopcock-molecules can be used simply to quantitatively
34 seal the channels^{38,136} but also to provide a gate for specific communication with an external object
35 (dyes,^{36,49} nanoclusters,¹³⁷ surfaces,^{17,42,138} bacteria^{52,139} etc.); see e.g. refs.^{1,35,36,38}. Although these
36 features explain why the tb-DXP-ZL composites are currently of very important technological
37 interest, there is certainly room for further progress in their performances and scopes. For example,
38 as it is known that the acidity inside of the ZL channels can cause problems,⁴⁸ an improvement of
39 the host matrix could be achieved by reducing the number of cations inside of the channels; e.g. by
40 reducing the 3.6 exchangeable cations per ZL unit cell to, e.g, about 2 exchangeable cations per unit
41 cell. Indeed, in dye-ZL based artificial antenna composites it is possible to achieve a maximum
42 loading of the donor molecules – which results in an extremely high speed for FRET and therefore
43 extremely high speed for exciton transport – but a low loading of acceptor molecules. The low
44 loading of acceptor molecules ensures a minimum of self-absorption losses and the high loading of
45 donor molecules guarantees a high rate of exciton transport so that the acceptors can quantitatively
46
47
48
49
50
51
52
53
54
55
56
57
58
59
60

1
2
3 capture the excitation energy. The best antenna systems that have been prepared so far make use of
4 tb-DXP as donor molecules. Nearly quantitative transfer to the acceptors has been reached (see e.g.
5 Figures 8 and 9 of ref.⁸⁹; Figure 4 and Table 2 in ref.⁴⁸; and Table 3 and Figure 9 in ref.⁴⁶).
6 Actually, the loading of tb-DXP was however less than about 50% in most examples. The inability
7 to realize higher loadings was due to thermal stability problems in the synthesis procedure. The
8 thermal stability of the acceptors (hostasol red) and of the imidazolium cation (IMZ⁺) needed to
9 reduce the acidity of the ZL matrix did not allow to apply the high temperature regime needed for
10 very high donor (tb-DXP) concentrations.⁴⁸ Finding thermally more robust acceptors, or something
11 more robust than IMZ⁺ to reduce the acidity, would allow to realize antenna systems with an even
12 greater tb-DXP loading. Although this goal still remains a challenge, the systems synthesized so far
13 are good enough for technical applications and represent a motivation towards further advances.
14 Accordingly, and in light of the results obtained in the present work, other viable strategies to
15 improve the guest could comprise the addition of C=O anchor groups (which increase the stability
16 of the host-guest material),⁵⁷ the inclusion of bulky end groups (to decrease the likelihood of
17 intermolecular coupling),¹⁸ or the addition of long unsaturated chains (to improve molecular
18 mobility in the ZL-channels).⁸⁹

19 The realization and optimization of the energy transfer and optical properties strictly relies on a
20 detailed understanding of the microscopic structure of the hybrid composites, because subtle
21 changes of the host-guest and guest-guest interactions can affect their functionality. Tb-DXP is one
22 of the most important dyes that have been used so far for preparing dye-ZL composites (see e.g.
23 ref.¹⁸). It is evident that a detailed understanding of the structure and interactions of tb-DXP/ZL
24 composites as achieved in the present study is key for allowing future progress of these materials.
25 Particularly in the latest years, due to the exponential increase in computational capacities, high-
26 accuracy simulations of zeolite-based materials have become possible,⁸² and modeling studies have
27 proven to be an essential tool to help addressing these issues.⁸¹ Indeed, besides unraveling the
28 atomistic-level structure and working mechanisms of various dye-ZL hybrids at operating
29 conditions,^{57-60,65,67,74,140,141} computational studies also shed light on the host-guest interactions
30 underlying the interface chemistry of these compounds, including phenomena of key relevance in
31 practical applications, like the incorporation of guest molecules during the preparation of the hybrid
32 composites⁸³ and the site-specific modification of the channel entrances of the host matrix.³⁸ As a
33 matter of fact, the atomistic knowledge of stopcock-functionalized ZL channel entrances³⁸ was
34 instrumental for the successful incorporation of the indigo dye in ZL, leading to a totally new type
35 of colorant endowed with an impressive resilience to harsh conditions.¹³⁶ Furthermore, theoretical
36 modeling has been also successfully exploited to predict host-guest behaviour under extreme
37
38
39
40
41
42
43
44
45
46
47
48
49
50
51
52
53
54
55
56
57
58
59
60

1
2
3 conditions, such as the pressure-driven formation of organized supramolecular patterns in
4 framework materials.⁶⁶ In view of these established facts, and of the unvaluable insight provided
5 herein by simulations – which rationalized all experimental evidences into a coherent, unifying
6 picture - it is straightforward to foresee, for the next future, a growing relevance of theoretical
7 modeling in the broader field of host-guest functional materials.
8
9

10 11 12 **Conclusions**

13
14 In this work, we determined the structure of self-assembled composites of zeolite L with the
15 perylene-diimide dye tb-DXP, revealing the fundamental host-guest interactions at atomistic-level
16 detail. We found that tb-DXP is positioned with its widest parts in the widest portions of the ZL
17 channel, and shows, unexpectedly, a slightly asymmetric arrangement with respect to the channel
18 center, both with and without water. This arrangement is affected by water only to a minor extent.
19 The main structural effects of hydration are: i) the out-of-plane distortion of the perylene core, and
20 ii) a slight increase of the separation of the dye from potassium cations, and hence from ZL channel
21 walls. The supramolecular organization of tb-DXP in ZL is determined by two types of
22 contributions: the leading one is related to shape-volume constraints, while the second one to the
23 relative strength of competitive interactions involving ZL, the dye, water molecules, and charge-
24 balancing cations. This knowledge can be used to improve the performance of this class of
25 technologically relevant hybrid materials, for example through the addition of C=O anchor groups,
26 or the inclusion of bulky end substituents /long unsaturated chains to the perylene-diimide dye.
27

28 In conclusion, we have solved and rationalized at atomistic level the structure of the zeolite L
29 composite with the perylene-diimide dye tb-DXP. We achieved this goal via a multi-techniques
30 approach: while the fundamental contribution of modeling was already recognized in the literature,
31 we have shown that its integration with diverse experiments characterized by different times scale
32 and focusing on different observables has provided a microscopically detailed picture of such
33 complex system, thus allowing to accommodate seemingly contrasting experimental evidences into
34 a unitary, and thoroughly consistent description of the supramolecular chemistry of these
35 technologically relevant hybrid materials. In view of its predictive power, the theoretical-
36 experimental approach used in this work can be thus applied to the implementation of improved
37 host-guest systems enabling for even greater FRET efficiencies. In a wider perspective, the insight
38 gathered from this study contributes to the general understanding of the interplay of host guest
39 interactions leading to stable dye-ZL hybrids composites, which is a necessary step to get control
40 over the subtle, finely-tuned mechanisms of these confined supramolecular assemblies of amazing
41 complexity in order to further extend their application scope.
42
43
44
45
46
47
48
49
50
51
52
53
54
55
56
57
58
59
60

ASSOCIATED CONTENT

Supporting Information

Atomic coordinates, occupancy factors and thermal displacement parameters for the structures of hydrated ZL/tb-DXP and anhydrous ZL/tb-DXP composites. Extraframework bond distances $< 4 \text{ \AA}$ for hydrated ZL/tb-DXP and anhydrous ZL/tb-DXP composites from Rietveld refinements. Observed and calculated diffraction patterns and final difference curve from Rietveld refinements of hydrated ZL/tb-DXP and anhydrous ZL/tb-DXP composites. View along [001] and along [100] of the arrangement of the tb-DXP and water molecules in the composite as obtained by Rietveld refinements. View along [100] of the arrangement model of the tb-DXP molecule within the ZL channel in the dry form, as obtained from structural refinements. Selected geometrical parameters of tb-DXP calculated at different levels of theory. Snapshots of the graphical representations of the calculated vibrational normal modes for an isolated tb-DXP molecule. IR spectra of anhydrous ZL/tb-DXP at room temperature with D₂O vapor at increasing pressure. Fluorescence emission and excitation spectra of ZL/tb-DXP in the hydrated and anhydrous forms. Full Reference for Gaussian 09. This material is available free of charge via the Internet at

AUTHOR INFORMATION

Corresponding Authors

Dr Lara Gigli
Elettra-Sincrotrone, SS14, Science Park, I-34149, Basovizza-Trieste (Italy)
e-mail: lara.gigli@elettra.eu

Prof. Ettore Fois
Dipartimento di Scienza e Alta Tecnologia, Insubria University, Via Valleggio 11, I-22100 Como (Italy)
e-mail: ettore.fois@uninsubria.it

Notes

The authors declare no competing financial interest.

Acknowledgements

The BM01 beamline at the European Synchrotron Radiation Facility and Dr. Vladimir Dmitriev are acknowledged for allocation of experimental beamtime. Carlotta Giacobbe is acknowledged for the data collection at ID22 beamline. Andrea Bernasconi is acknowledged for the help in the total scattering data analysis and for constructive discussions. Dr. Simona Bigi is acknowledged for the help in TGA-MSEGA analyses. Three anonymous referees are acknowledged for insightful comments and suggestions. This work was supported by the Italian MIUR, (PRIN2015 “ZAPPING” High-pressure nano-confinement in Zeolites: the Mineral Science know-how APPLIED to engineerING of innovative materials for technological and environmental applications” 2015HK93L7), ImPACT (FIRB RBF12CLQD) and by Insubria University (FAR 2015-2016).

- (1) Calzaferri, G. Nanochannels: Hosts for the Supramolecular Organization of Molecules and Complexes. *Langmuir* **2012**, *28*, 6216–6231.
- (2) Schulz-Ekloff, G.; Wöhrle, D.; van Duffel, B.; Schoonheydt, R. A. Chromophores in Porous Silicas and Minerals: Preparation and Optical Properties. *Microporous Mesoporous Mater.* **2002**, *51*, 91–138.
- (3) Corma, A.; Garcia, H. Supramolecular Host-Guest Systems in Zeolites Prepared by Ship-in-a-Bottle Synthesis. *Eur. J. Inorg. Chem.* **2004**, *2004*, 1143–1164.
- (4) Calzaferri, G.; Lutkouskaya, K. Mimicking the Antenna System of Green Plants. *Photochem. Photobiol. Sci.* **2008**, *7*, 879–910.
- (5) Calzaferri, G.; Huber, S.; Maas, H.; Minkowski, C. Host-Guest Antenna Materials. *Angew. Chem., Int. Ed.* **2003**, *42*, 3732–3758.
- (6) Yoon, K. B. Organization of Zeolite Microcrystals for Production of Functional Materials. *Acc. Chem. Res.* **2007**, *40*, 29–40.
- (7) Alarcos, N.; Cohen, B.; Ziółek, M.; Douhal, A. Photochemistry and Photophysics in Silica-Based Materials: Ultrafast and Single Molecule Spectroscopy Observation. *Chem. Rev.* **2017**, *117*, 13639–13720.
- (8) Maggini, L.; Bonifazi, D. Hierarchised Luminescent Organic Architectures: Design, Synthesis, Self-Assembly, Self-Organisation and Functions. *Chem. Soc. Rev.* **2012**, *41*, 211–241.
- (9) Lencione, D.; Gehlen, M. H.; Trujillo, L. N.; Leitao, R. C. F.; Albuquerque, R. Q. The Spatial Distribution of the Photostability of Thionine in Zeolite L Nanochannels Investigated

- 1
2
3 by Photobleaching Lifetime Imaging Microscopy. *Photochem. Photobiol. Sci.* **2016**, *1*, 398–
4 404.
5
6 (10) Gartzia-Rivero, L.; Bañuelos, J.; López-Arbeloa, I. Excitation Energy Transfer in Artificial
7 Antennas: From Photoactive Materials to Molecular Assemblies. *Int. Rev. Phys. Chem.* **2015**,
8 *34*, 515–556.
9
10 (11) Rao, K. V.; Jain, A.; George, S. J. Organic–inorganic Light-Harvesting Scaffolds for
11 Luminescent Hybrids. *J. Mater. Chem. C* **2014**, *2*, 3055–3064.
12
13 (12) Barrer, R. M.; Villiger, H. The Crystal Structure of the Synthetic Zeolite L. *Zeitschrift für*
14 *Krist. - Cryst. Mater.* **1969**, *128*, 352–370.
15
16 (13) Calzaferri, G.; Gfeller, N. Thionine in the Cage of Zeolite L. *J. Phys. Chem.* **1992**, *96*, 3428–
17 3435.
18
19 (14) Ramamurthy, V.; Mondal, B. Supramolecular Photochemistry Concepts Highlighted with
20 Select Examples. *J. Photochem. Photobiol. C Photochem. Rev.* **2015**, *23*, 68–102.
21
22 (15) Pauchard, M.; Huber, S.; Méallet-Renault, R.; Maas, H.; Pansu, R.; Calzaferri, G. Time- and
23 Space-Resolved Luminescence of a Photonic Dye-Zeolite Antenna. *Angew. Chem., Int. Ed.*
24 **2001**, *40*, 2839–2842.
25
26 (16) Hashimoto, S.; Hagiri, M.; Matsubara, N.; Tobita, S. Photophysical Studies of Neutral
27 Aromatic Species Confined in Zeolite L: Comparison with Cationic Dyes. *Phys. Chem.*
28 *Chem. Phys.* **2001**, *3*, 5043–5051.
29
30 (17) Wang, Y.; Li, H.; Feng, Y.; Zhang, H.; Calzaferri, G.; Ren, T. Orienting Zeolite L
31 Microcrystals with a Functional Linker. *Angew. Chem., Int. Ed.* **2010**, *49*, 1434–1438.
32
33 (18) Calzaferri, G.; Méallet-Renault, R.; Brühwiler, D.; Pansu, R.; Dolamic, I.; Dienel, T.; Adler,
34 P.; Li, H.; Kunzmann, A. Designing Dye-Nanochannel Antenna Hybrid Materials for Light
35 Harvesting, Transport and Trapping. *ChemPhysChem* **2011**, *12*, 580–594.
36
37 (19) Brühwiler, D.; Calzaferri, G.; Torres, T.; Ramm, J. H.; Gartmann, N.; Dieu, L.-Q.; López-
38 Duarte, I.; Martínez-Díaz, M. V. Nanochannels for Supramolecular Organization of
39 Luminescent Guests. *J. Mater. Chem.* **2009**, *19*, 8040–8067.
40
41 (20) Hu, D.-D.; Wang, L.; Lin, J.; Bu, F.; Wu, T. Tuning the Efficiency of Multi-Step Energy
42 Transfer in a Host–guest Antenna System Based on a Chalcogenide Semiconductor Zeolite
43 through Acidification and Solvation of Guests. *J. Mater. Chem. C* **2015**, *3*, 11747–11753.
44
45 (21) Kehr, N. S.; Motealleh, A.; Schäfer, A. H. Cell Growth on (“Janus”) Density Gradients of
46 Bifunctional Zeolite L Crystals. *ACS Appl. Mater. Interfaces* **2016**, *8*, 35081–35090.
47
48 (22) Kim, D.; Kim, H. S. Enhancement of Fluorescence from One- and Two-Photon Absorption
49 of Hemicyanine Dyes by Confinement in Silicalite-1 Nanochannels. *Microporous*
50
51
52
53
54
55
56
57
58
59
60

- 1
2
3 *Mesoporous Mater.* **2017**, *243*, 69–75.
- 4 (23) Sola-Llano, R.; Fujita, Y.; Gómez-Hortigüela, L.; Alfayate, A.; Ujii, H.; Fron, E.; Toyouchi,
5 S.; Perez-Pariente, J.; Lopez-Arbeloa, I.; Martinez-Martinez, V. One-Directional Antenna
6 Systems: Energy Transfer from Monomers to J-Aggregates within 1D Nanoporous
7 Aluminophosphates. *ACS Photonics* **2017**, doi: 10.1021/acsp Photonics.7b00553.
- 8
9 (24) Kittikhunnatham, P.; Som, B.; Rassolov, V.; Stolte, M.; Würthner, F.; Shimizu, L. S.;
10 Greytak, A. B. Fluorescence Polarization Measurements to Probe Alignment of a
11 Bithiophene Dye in One-Dimensional Channels of Self-Assembled Phenylethynylene Bis-
12 Urea Macrocyclic Crystals. *J. Phys. Chem. C* **2017**, *121*, 18102–18109.
- 13
14 (25) Onida, B.; Bonelli, B.; Flora, L.; Geobaldo, F.; Areal, C. O.; Garrone, E. Permeability of
15 Micelles in Surfactant-Containing MCM-41 Silica as Monitored by Embedded Dye
16 Molecules. *Chem. Commun.* **2001**, 2216–2217.
- 17
18 (26) Cucinotta, F.; Carniato, F.; Devaux, A.; De Cola, L.; Marchese, L. Efficient Photoinduced
19 Energy Transfer in a Newly Developed Hybrid SBA-15 Photonic Antenna. *Chem. - A Eur. J.*
20 **2012**, *18*, 15310–15315.
- 21
22 (27) Grösch, L.; Lee, Y. J.; Hoffmann, F.; Fröba, M. Light-Harvesting Three-Chromophore
23 Systems Based on Biphenyl-Bridged Periodic Mesoporous Organosilica. *Chem. - A Eur. J.*
24 **2015**, *21*, 331–346.
- 25
26 (28) Noh, T. H.; Jang, J.; Hong, W.; Lee, H.; Jung, O.-S. Truncated Trigonal Prismatic Tubular
27 Crystals Consisting of a Zeolite L-Mimic Metal-Organic Framework. *Chem. Commun.* **2014**,
28 *56*, 7451–7454.
- 29
30 (29) Yu, J.; Cui, Y.; Wu, C.; Yang, Y.; Wang, Z.; O’Keeffe, M.; Chen, B.; Qian, G. Second-Order
31 Nonlinear Optical Activity Induced by Ordered Dipolar Chromophores Confined in the Pores
32 of an Anionic Metal-Organic Framework. *Angew. Chem., Int. Ed.* **2012**, *51*, 10542–10545.
- 33
34 (30) Handke, M.; Adachi, T.; Hu, C.; Ward, M. D. Encapsulation of Isolated Luminophores
35 within Supramolecular Cages. *Angew. Chem., Int. Ed.* **2017**, *56*, 14003-14006.
- 36
37 (31) Martínez-Martínez, V.; García, R.; Gómez-Hortigüela, L.; Sola Llano, R.; Pérez-Pariente, J.;
38 López-Arbeloa, I. Highly Luminescent and Optically Switchable Hybrid Material by One-Pot
39 Encapsulation of Dyes into MgAPO-11 Unidirectional Nanopores. *ACS Photonics* **2014**, *1*,
40 205–211.
- 41
42 (32) Epelde-Elezcano, N.; Martínez-Martínez, V.; Duque-Redondo, E.; Temiño, I.; Manzano, H.;
43 López-Arbeloa, I. Strategies for Modulating the Luminescence Properties of Pyronin Y Dye–
44 Clay Films: An Experimental and Theoretical Study. *Phys. Chem. Chem. Phys.* **2016**, *18*,
45 8730–8738.
- 46
47
48
49
50
51
52
53
54
55
56
57
58
59
60

- 1
2
3 (33) Olivero, F.; Carniato, F.; Bisio, C.; Marchese, L. Promotion of Förster Resonance Energy
4 Transfer in a Saponite Clay Containing Luminescent Polyhedral Oligomeric Silsesquioxane
5 and Rhodamine Dye. *Chem. - An Asian J.* **2014**, *9*, 158–165.
- 6
7 (34) Costantino, U.; Costantino, F.; Elisei, F.; Latterini, L.; Nocchetti, M. Coupling Physical
8 Chemical Techniques with Hydrotalcite-like Compounds to Exploit Their Structural Features
9 and New Multifunctional Hybrids with Luminescent Properties. *Phys. Chem. Chem. Phys.*
10 **2013**, *15*, 13254–13269.
- 11
12 (35) Maas, H.; Calzaferri, G. Trapping Energy from and Injecting Energy into Dye-Zeolite
13 Nanoantennae. *Angew. Chem., Int. Ed.* **2002**, *41*, 2284–2288.
- 14
15 (36) López-Duarte, I.; Le-Quyenha Dieu; Dolamic, I.; Martínez-Díaz, M. V.; Torres, T.;
16 Calzaferri, G.; Brühwiler, D. On the Significance of the Anchoring Group in the Design of
17 Antenna Materials Based on Phthalocyanine Stopcocks and Zeolite L. *Chem. - A Eur. J.*
18 **2011**, *16*, 1855–1862.
- 19
20 (37) Li, P.; Wang, Y.; Li, H.; Calzaferri, G. Luminescence Enhancement after Adding Stoppers to
21 europium(III) Nanozeolite L. *Angew. Chem., Int. Ed.* **2014**, *53*, 2904–2909.
- 22
23 (38) Tabacchi, G.; Fois, E.; Calzaferri, G. Structure of Nanochannel Entrances in Stopcock-
24 Functionalized Zeolite L Composites. *Angew. Chem., Int. Ed.* **2015**, *54*, 11112–11116.
- 25
26 (39) Li, H.; Wang, Y.; Zhang, W.; Liu, B.; Calzaferri, G. Fabrication of Oriented Zeolite L
27 Monolayers Employing Luminescent Perylenediimide-Bridged Silsesquioxane Precursor as
28 the Covalent Linker. *Chem. Commun.* **2007**, 2853–2854.
- 29
30 (40) Lee, J. S.; Lim, H.; Ha, K.; Cheong, H.; Yoon, K. B. Facile Monolayer Assembly of
31 Fluorophore-Containing Zeolite Rods in Uniform Orientations for Anisotropic
32 Photoluminescence. *Angew. Chem., Int. Ed.* **2006**, *45*, 5288–5292.
- 33
34 (41) El-Gindi, J.; Benson, K.; De Cola, L.; Galla, H. J.; Seda Kehr, N. Cell Adhesion Behavior on
35 Enantiomerically Functionalized Zeolite L Monolayers. *Angew. Chem., Int. Ed.* **2012**, *51*,
36 3716–3720.
- 37
38 (42) Ruiz, A. Z.; Li, H.; Calzaferri, G. Organizing Supramolecular Functional Dye-Zeolite
39 Crystals. *Angew. Chem., Int. Ed.* **2006**, *45*, 5282–5287.
- 40
41 (43) Vohra, V.; Calzaferri, G.; Destri, S.; Pasini, M.; Porzio, W.; Botta, C. Toward White Light
42 Emission through Efficient Two-Step Energy Transfer in Hybrid Nanofibers. *ACS Nano*
43 **2010**, *4*, 1409–1416.
- 44
45 (44) Beierle, J. M.; Roswanda, R.; Erne, P. M.; Coleman, A. C.; Browne, W. R.; Feringa, B. L.
46 An Improved Method for Site-Specific End Modification of Zeolite L for the Formation of
47 Zeolite L and Gold Nanoparticle Self-Assembled Structures. *Part. Part. Syst. Charact.* **2013**,

- 1
2
3 30, 273–279.
- 4 (45) Busby, M.; Devaux, A.; Blum, C.; Subramaniam, V.; Calzaferri, G.; De Cola, L. Interactions
5 of Perylene Bisimide in the One-Dimensional Channels of Zeolite L. *J. Phys. Chem. C* **2011**,
6 *115*, 5974–5988.
- 7
8
9 (46) Devaux, A.; Calzaferri, G.; Miletto, I.; Cao, P.; Belser, P.; Brühwiler, D.; Khorev, O.; Häner,
10 R.; Kunzmann, A. Self-Absorption and Luminescence Quantum Yields of Dye-Zeolite L
11 Composites. *J. Phys. Chem. C* **2013**, *117*, 23034–23047.
- 12
13
14 (47) Li, P.; Zhang, Y.; Wang, Y.; Wang, Y.; Li, H. Luminescent Europium(III)- β -Diketonate
15 Complexes Hosted in Nanozeolite L as Turn-on Sensors for Detecting Basic Molecules.
16 *Chem. Commun.* **2014**, *50*, 13680–13682.
- 17
18
19 (48) Devaux, A.; Calzaferri, G.; Belser, P.; Cao, P.; Brühwiler, D.; Kunzmann, A. Efficient and
20 Robust Host-Guest Antenna Composite for Light Harvesting. *Chem. Mater.* **2014**, *26*, 6878–
21 6885.
- 22
23
24 (49) Gartzia-Rivero, L.; Bañuelos, J.; López-Arbeloa, I. Photoactive Nanomaterials Inspired by
25 Nature: LTL Zeolite Doped with Laser Dyes as Artificial Light Harvesting Systems.
26 *Materials* **2017**, *10*, 495.
- 27
28
29 (50) Fibikar, S.; Luppi, G.; Martínez-Junza, V.; Clemente-León, M.; De Cola, L. Manipulation
30 and Orientation of Zeolite L by Using a Magnetic Field. *ChemPlusChem* **2015**, *80*, 62–67.
- 31
32 (51) Cucinotta, F.; Guenet, A.; Bizzarri, C.; Mroz, W.; Botta, C.; Milian-Medina, B.; Gierschner,
33 J.; De Cola, L. Energy Transfer at the Zeolite L Boundaries: Towards Photo- and
34 Electroresponsive Materials. *ChemPlusChem* **2014**, *79*, 45–57.
- 35
36
37 (52) Popović, Z.; Otter, M.; Calzaferri, G.; De Cola, L. Self-Assembling Living Systems with
38 Functional Nanomaterials. *Angew. Chem., Int. Ed.* **2007**, *46*, 6188–6191.
- 39
40 (53) De Cremer, G.; Sels, B. F.; De Vos, D. E.; Hofkens, J.; Roeyers, M. B. J. Fluorescence
41 Micro(spectro)scopy as a Tool to Study Catalytic Materials in Action. *Chem. Soc. Rev.* **2010**,
42 *39*, 4703–4717.
- 43
44
45 (54) Domke, K. F.; Day, J. P. R.; Rago, G.; Riemer, T. A.; Kox, M. H. F.; Weckhuysen, B. M.;
46 Bonn, M. Host-Guest Geometry in Pores of Zeolite ZSM-5 Spatially Resolved with
47 Multiplex CARS Spectromicroscopy. *Angew. Chem., Int. Ed.* **2012**, *51*, 1343–1347.
- 48
49 (55) Hendriks, F. C.; Schmidt, J. E.; Rombouts, J. A.; Lammertsma, K.; Bruijninx, P. C. A.;
50 Weckhuysen, B. M. Probing Zeolite Crystal Architecture and Structural Imperfections Using
51 Differently Sized Fluorescent Organic Probe Molecules. *Chem. - A Eur. J.* **2017**, *23*, 6305–
52 6314.
- 53
54
55
56 (56) Liao, Y.-Y.; Melissen, S. T. A. G.; Audibert, J.-F.; Vu, T.-T.; Clavier, G.; Méallet-Renault,

- R.; Retailleau, P.; Lemaistre, J.-P.; Génot, V.; Pansu, R. Fluorescence Spectroscopy of AdamBODIPY Single Crystals. *ChemPhotoChem* **2017**, doi: 10.1002/cptc.201700173.
- (57) Fois, E.; Tabacchi, G.; Calzaferri, G. Interactions, Behavior, and Stability of Fluorenone inside Zeolite Nanochannels. *J. Phys. Chem. C* **2010**, *114*, 10572–10579.
- (58) Zhou, X.; Wesolowski, T. A.; Tabacchi, G.; Fois, E.; Calzaferri, G.; Devaux, A. First-Principles Simulation of the Absorption Bands of Fluorenone in Zeolite L. *Phys. Chem. Chem. Phys.* **2013**, *15*, 159–167.
- (59) Fois, E.; Tabacchi, G.; Calzaferri, G. Orientation and Order of Xanthene Dyes in the One-Dimensional Channels of Zeolite L: Bridging the Gap between Experimental Data and Molecular Behavior. *J. Phys. Chem. C* **2012**, *116*, 16784–16799.
- (60) Fois, E.; Tabacchi, G.; Devaux, A.; Belser, P.; Brühwiler, D.; Calzaferri, G. Host-Guest Interactions and Orientation of Dyes in the One-Dimensional Channels of Zeolite L. *Langmuir* **2013**, *29*, 9188–9198.
- (61) Baerlocher, C.; McCusker, L. B.; Olson, D. H. *Atlas of Zeolite Framework Types*; Published on behalf of the Structure Commission of the International Zeolite Association by Elsevier, 2007.
- (62) Hoppe, R.; Schulz-Ekloff, G.; Wöhrle, D.; Kirschhock, C.; Fuess, H.; Uytterhoeven, L.; Schoonheydt, R. Incorporation of Methylene Blue in NaY Zeolite at Crystallographically Defined Positions. *Adv. Mater.* **1995**, *7*, 61–64.
- (63) Hennessy, B.; Megelski, S.; Marcolli, C.; Shklover, V.; Baerlocher, C.; Calzaferri, G. Characterization of Methyl Viologen in the Channels of Zeolite L. *J. Phys. Chem. B* **1999**, *103*, 3340–3351.
- (64) Simoncic, P.; Armbruster, T. Cationic Methylene Blue Incorporated into Zeolite Mordenite-Na: A Single Crystal X-Ray Study. *Microporous Mesoporous Mater.* **2005**, *81*, 87–95.
- (65) Gigli, L.; Arletti, R.; Tabacchi, G.; Fois, E.; Vitillo, J. G.; Martra, G.; Agostini, G.; Quartieri, S.; Vezzalini, G. Close-Packed Dye Molecules in Zeolite Channels Self-Assemble into Supramolecular Nanoladders. *J. Phys. Chem. C* **2014**, *118*, 15732–15743.
- (66) Arletti, R.; Fois, E.; Gigli, L.; Vezzalini, G.; Quartieri, S.; Tabacchi, G. Irreversible Conversion of a Water–Ethanol Solution into an Organized Two-Dimensional Network of Alternating Supramolecular Units in a Hydrophobic Zeolite under Pressure. *Angew. Chem., Int. Ed.* **2017**, *56*, 2105–2109.
- (67) Manzano, H.; Gartzia-Rivero, L.; Bañuelos, J.; López-Arbeloa, I. Ultraviolet-Visible Dual Absorption by Single BODIPY Dye Confined in LTL Zeolite Nanochannels. *J. Phys. Chem. C* **2013**, *117*, 13331–13336.

- 1
2
3 (68) Fois, E.; Gamba, A.; Medici, C.; Tabacchi, G. Intermolecular Electronic Excitation Transfer
4 in a Confined Space: A First-Principles Study. *ChemPhysChem* **2005**, *6*, 1917–1922.
- 5
6 (69) Bussemer, B.; Munsel, D.; Wünsch, H.; Mohr, G. J.; Grummt, U. W. Electronic Properties
7 of Neutral Dyes in the Channels of Zeolite L: A Combined Spectroscopic and Quantum
8 Chemical Study. *J. Phys. Chem. B* **2007**, *111*, 8–15.
- 9
10 (70) Fois, E.; Gamba, A.; Spano, E.; Tabacchi, G. Rotation of Molecules and Ions in Confined
11 Spaces: A First-Principles Simulation Study. *J. Mol. Struct.* **2003**, *644*, 55–66.
- 12
13 (71) Fois, E.; Gamba, A.; Tilocca, A. On the Unusual Stability of Maya Blue Paint: Molecular
14 Dynamics Simulations. *Microporous Mesoporous Mater.* **2003**, *57*, 263–272.
- 15
16 (72) Giustetto, R.; Seenivasan, K.; Bonino, F.; Ricchiardi, G.; Bordiga, S.; Chierotti, M. R.;
17 Gobetto, R. Host/guest Interactions in a Sepiolite-Based Maya Blue Pigment: A
18 Spectroscopic Study. *J. Phys. Chem. C* **2011**, *115*, 16764–16776.
- 19
20 (73) Spanó, E.; Tabacchi, G.; Gamba, A.; Fois, E. On the Role of Ti(IV) as a Lewis Acid in the
21 Chemistry of Titanium Zeolites: Formation, Structure, Reactivity, and Aging of Ti-Peroxo
22 Oxidizing Intermediates. A First Principles Study. *J. Phys. Chem. B* **2006**, *110*, 21651–
23 21661.
- 24
25 (74) Insuwan, W.; Rangriwatananon, K.; Meeprasert, J.; Namuangruk, S.; Surakhot, Y.;
26 Kungwan, N.; Jungstittiwong, S. Combined Experimental and Theoretical Investigation on
27 Fluorescence Resonance Energy Transfer of Dye Loaded on LTL Zeolite. *Microporous
28 Mesoporous Mater.* **2017**, *241*, 372–382.
- 29
30 (75) Gamba, A.; Tabacchi, G.; Fois, E. TS-1 from First Principles. *J. Phys. Chem. A* **2009**, *113*,
31 15006–15015.
- 32
33 (76) Calzaferri, G. Entropy in Multiple Equilibria, Theory and Applications. *Phys. Chem. Chem.
34 Phys.* **2017**, *19*, 10611–10621.
- 35
36 (77) Fois, E.; Gamba, A.; Medici, C.; Tabacchi, G.; Quartieri, S.; Mazzucato, E.; Arletti, R.;
37 Vezzalini, G.; Dmitriev, V. High Pressure Deformation Mechanism of Li-ABW: Synchrotron
38 XRPD Study and Ab Initio Molecular Dynamics Simulations. *Microporous Mesoporous
39 Mater.* **2008**, *115*, 267–280.
- 40
41 (78) Choudhary, A.; Das, B.; Ray, S. Encapsulated Schiff Base Nickel Complex in Zeolite Y:
42 Correlation between Catalytic Activities and Extent of Distortion Supported by Experimental
43 and DFT Studies. *Inorganica Chim. Acta* **2017**, *462*, 256–265.
- 44
45 (79) Doungmanee, S.; Siritanon, T.; Insuwan, W.; Jungstittiwong, S.; Rangriwatananon, K. Multi
46 Step Energy Transfer between Three Si_LTL and SiGe_LTL Zeolite-Loaded Dyes. *J. Porous
47 Mater.* **2017**, <https://doi.org/10.1007/s10934-017-0550-7>.
- 48
49
50
51
52
53
54
55
56
57
58
59
60

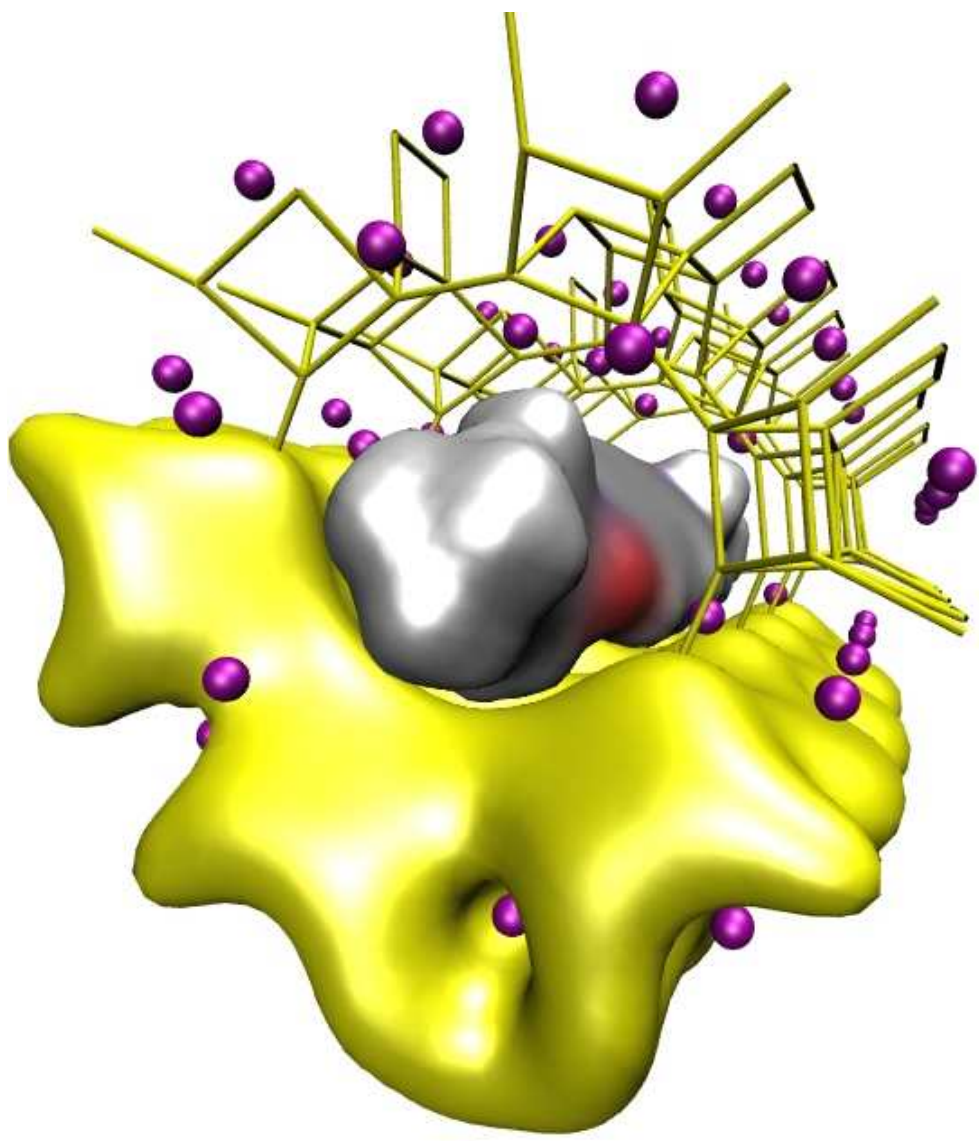
- 1
2
3 (80) Mohan, S. C.; Vijay Solomon, R.; Venuvanalingam, P.; Jothivenkatachalam, K.
4 Encapsulation of a Hexaaza Macrocyclic Nickel(II) Complex in Zeolite Y: An
5 Experimental and Theoretical Investigation. *New J. Chem.* **2017**, *41*, 9505–9512.
- 6
7 (81) Gatta, G. D.; Lotti, P.; Tabacchi, G. The Effect of Pressure on Open-Framework Silicates:
8 Elastic Behaviour and Crystal–fluid Interaction. *Phys. Chem. Miner.* **2017**, doi:
9 10.1007/s00269-017-0916-z.
10
11 (82) Van Speybroeck, V.; Hemelsoet, K.; Joos, L.; Waroquier, M.; Bell, R. G.; Catlow, C. R. A.
12 Advances in Theory and Their Application within the Field of Zeolite Chemistry. *Chem. Soc.*
13 *Rev.* **2015**, *44*, 7044–7111.
14
15 (83) Tabacchi, G.; Calzaferri, G.; Fois, E. One-Dimensional Self-Assembly of Perylene-Diimide
16 Dyes by Unidirectional Transit of Zeolite Channel Openings. *Chem. Commun.* **2016**, *52*,
17 11195–11198.
18
19 (84) Keen, D. A.; Goodwin, A. L. The Crystallography of Correlated Disorder. *Nature* **2015**, *521*,
20 303–309.
21
22 (85) Fois, E.; Tabacchi, G.; Barreca, D.; Gasparotto, A.; Tondello, E. “Hot” surface Activation of
23 Molecular Complexes: Insight from Modeling Studies. *Angew. Chem., Int. Ed.* **2010**, *49*,
24 1944–1948.
25
26 (86) Tabacchi, G.; Fois, E.; Barreca, D.; Gasparotto, A. Opening the Pandora’s Jar of Molecule-
27 to-Material Conversion in Chemical Vapor Deposition: Insights from Theory. *Int. J.*
28 *Quantum Chem.* **2014**, *114*, 1–7.
29
30 (87) Deiana, C.; Fois, E.; Martra, G.; Narbey, S.; Pellegrino, F.; Tabacchi, G. On the Simple
31 Complexity of Carbon Monoxide on Oxide Surfaces: Facet-Specific Donation and
32 Backdonation Effects Revealed on TiO₂ Anatase Nanoparticles. *ChemPhysChem* **2016**, *17*,
33 1956–1960.
34
35 (88) Würthner, F. Perylene Bisimide Dyes as Versatile Building Blocks for Functional
36 Supramolecular Architectures. *Chem. Commun.* **2004**, 1564–1579.
37
38 (89) Cao, P.; Khorev, O.; Devaux, A.; Sägesser, L.; Kunzmann, A.; Ecker, A.; Häner, R.;
39 Brühwiler, D.; Calzaferri, G.; Belser, P. Supramolecular Organization of Dye Molecules in
40 Zeolite L Channels: Synthesis, Properties, and Composite Materials. *Chem. - A Eur. J.* **2016**,
41 *22*, 4046–4060.
42
43 (90) Newsam, J. M. Structures of Dehydrated Potassium Zeolite L at 298 and 78K and at 78K
44 Containing Sorbed Perdeuteriobenzene. *J. Phys. Chem.* **1989**, *93*, 7689–7694.
45
46 (91) Hammersley, A. P.; Svensson, S. O.; Hanfland, M.; Fitch, A. N.; Hausermann, D. Two-
47 Dimensional Detector Software: From Real Detector to Idealised Image or Two-Theta Scan.
48
49
50
51
52
53
54
55
56
57
58
59
60

- 1
2
3 *High Press. Res.* **1996**, *14*, 235–248.
- 4 (92) Toby, B. H. EXPGUI, a Graphical User Interface for GSAS. *J. Appl. Crystallogr.* **2001**, *34*,
5 210–213.
- 6
7 (93) Kieffer, J.; Wright, J. P. PyFAI: A Python Library for High Performance Azimuthal
8 Integration on GPU. *Powder Diffr.* **2013**, *28*, S339–S350.
- 9
10 (94) Juhás, P.; Davis, T.; Farrow, C. L.; Billinge, S. J. L.; IUCr. *PDFgetX3* : A Rapid and Highly
11 Automatable Program for Processing Powder Diffraction Data into Total Scattering Pair
12 Distribution Functions. *J. Appl. Crystallogr.* **2013**, *46*, 560–566.
- 13
14 (95) Kortüm, G. *Reflectance Spectroscopy: Principles, Methods, Applications.*; Springer-Verlag:
15 Berlin, Heidelberg, 1969.
- 16
17 (96) Bandoli, G.; Barreca, D.; Gasparotto, A.; Seraglia, R.; Tondello, E.; Devi, A.; Fischer, R. A.;
18 Winter, M.; Fois, E.; Gamba, A.; et al. An Integrated Experimental and Theoretical
19 Investigation on Cu(hfa)₂·TMEDA: Structure, Bonding and Reactivity. *Phys. Chem. Chem.*
20 *Phys.* **2009**, *11*, 5998–6007.
- 21
22 (97) Fois, E.; Gamba, A.; Tabacchi, G. Structure and Dynamics of a Brønsted Acid Site in a
23 Zeolite: An Ab Initio Study of Hydrogen Sodalite. *J. Phys. Chem. B* **1998**, *102*, 3974–3979.
- 24
25 (98) Trudu, F.; Tabacchi, G.; Gamba, A.; Fois, E. First Principles Studies on Boron Sites in
26 Zeolites. *J. Phys. Chem. A* **2007**, *111*, 11626–11637.
- 27
28 (99) Tabacchi, G.; Silvi, S.; Venturi, M.; Credi, A.; Fois, E. Dethreading of a Photoactive
29 Azobenzene-Containing Molecular Axle from a Crown Ether Ring: A Computational
30 Investigation. *ChemPhysChem* **2016**, *17*, 1913–1919.
- 31
32 (100) Gatta, G. D.; Tabacchi, G.; Fois, E.; Lee, Y. Behaviour at High Pressure of
33 Rb₇NaGa₈Si₁₂O₄₀·3H₂O (a Zeolite with EDI Topology): A Combined Experimental–
34 computational Study. *Phys. Chem. Miner.* **2016**, *43*, 209–216.
- 35
36 (101) Martínez-Suarez, L.; Siemer, N.; Frenzel, J.; Marx, D. Reaction Network of Methanol
37 Synthesis over Cu/ZnO Nanocatalysts. *ACS Catal.* **2015**, *5*, 4201–4218.
- 38
39 (102) Fois, E.; Gamba, A.; Tabacchi, G.; Coluccia, S.; Martra, G. Ab Initio Study of Defect Sites at
40 the Inner Surfaces of Mesoporous Silicas. *J. Phys. Chem. B* **2003**, *107*, 10767–10772.
- 41
42 (103) Tabacchi, G.; Gianotti, E.; Fois, E.; Martra, G.; Marchese, L.; Coluccia, S.; Gamba, A.
43 Understanding the Vibrational and Electronic Features of Ti(IV) Sites in Mesoporous Silicas
44 by Integrated Ab Initio and Spectroscopic Investigations. *J. Phys. Chem. C* **2007**, *111*, 4946–
45 4955.
- 46
47 (104) Car, R.; Parrinello, M. Unified Approach for Molecular Dynamics and Density-Functional
48 Theory. *Phys. Rev. Lett.* **1985**, *55*, 2471–2474.
- 49
50
51
52
53
54
55
56
57
58
59
60

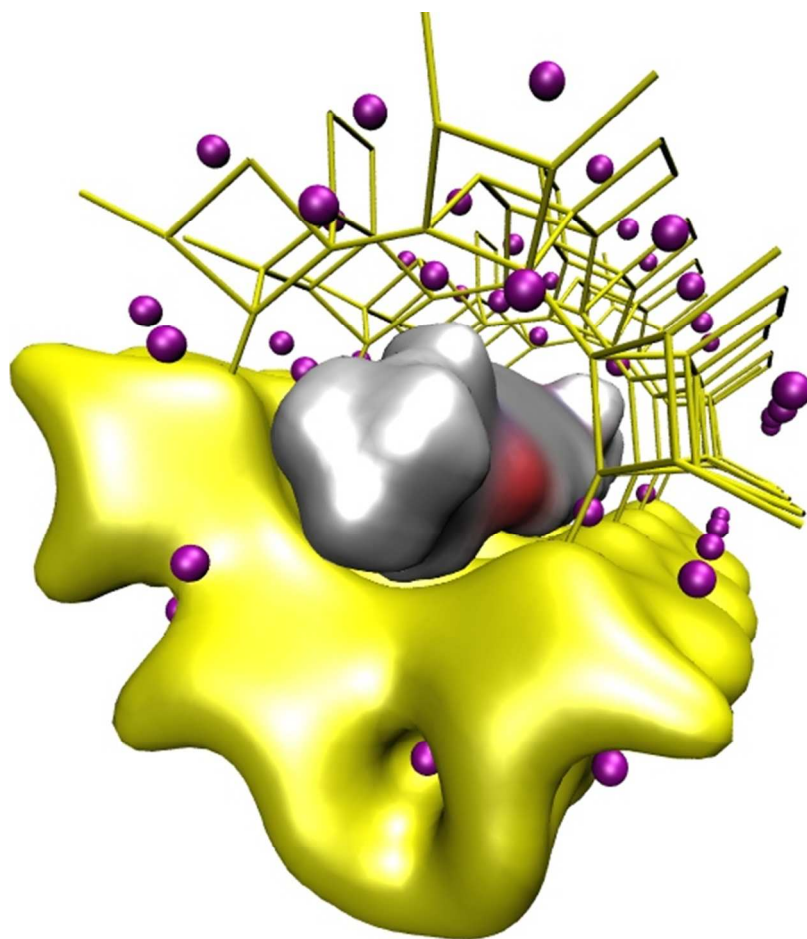
- 1
2
3 (105) IBM Corp. 1990–2017; MPI für Festkörperforschung Stuttgart 1997–2001. CPMD: Car
4 Parrinello Molecular Dynamics. 2017.
- 5
6 (106) Frisch, M. J.; Trucks, G. W.; Schlegel, H. B.; Scuseria, G. E.; Robb, M. A.; Cheeseman, J.
7 R.; Scalmani, G.; Barone, V.; Mennucci, B.; Petersson, G. A., et al. Gaussian 09, Revision
8 E.01,. Gaussian, Inc.: Wallingford CT 2009.
- 9
10 (107) Demontis, P.; Jobic, H.; Gonzalez, M. A.; Suffritti, G. B. Diffusion of Water in Zeolites NaX
11 and NaY Studied by Quasi-Elastic Neutron Scattering and Computer Simulation. *J. Phys.*
12 *Chem. C* **2009**, *113*, 12373–12379.
- 13
14 (108) Fois, E.; Gamba, A.; Tabacchi, G.; Arletti, R.; Quartieri, S.; Vezzalini, G. The “template”
15 effect of the Extra-Framework Content on Zeolite Compression: The Case of Yugawaralite.
16 *Am. Mineral.* **2005**, *90*, 28–35.
- 17
18 (109) Larin, A. V.; Trubnikov, D. N.; Vercauteren, D. P. Improvement of X-Ray Diffraction
19 Geometries of Water Physisorbed in Zeolites on the Basis of Periodic Hartree-Fock
20 Calculations. *Int. J. Quantum Chem.* **2005**, *102*, 971–979.
- 21
22 (110) Ferro, O.; Quartieri, S.; Vezzalini, G.; Fois, E.; Gamba, A.; Tabacchi, G. High-Pressure
23 Behavior of Bikitaite: An Integrated Theoretical and Experimental Approach. *Am. Mineral.*
24 **2002**, *87*, 1415–1425.
- 25
26 (111) Fischer, M. Structure and Bonding of Water Molecules in Zeolite Hosts: Benchmarking
27 Plane-Wave DFT against Crystal Structure Data. *Zeitschrift für Krist. - Cryst. Mater.* **2015**,
28 *230*, 325–336.
- 29
30 (112) Betti, C.; Fois, E.; Mazzucato, E.; Medici, C.; Quartieri, S.; Tabacchi, G.; Vezzalini, G.;
31 Dmitriev, V. Gismondine under HP: Deformation Mechanism and Re-Organization of the
32 Extra-Framework Species. *Microporous Mesoporous Mater.* **2007**, *103*, 190–209.
- 33
34 (113) Coudert, F.-X.; Cailliez, F.; Vuilleumier, R.; Fuchs, A. H.; Boutin, A. Water Nanodroplets
35 Confined in Zeolite Pores. *Faraday Discuss.* **2009**, *141*, 377–398.
- 36
37 (114) Fraux, G.; Coudert, F.-X.; Boutin, A.; Fuchs, A. H. Forced Intrusion of Water and Aqueous
38 Solutions in Microporous Materials: From Fundamental Thermodynamics to Energy Storage
39 Devices. *Chem. Soc. Rev.* **2017**, *46*, 7421–7437.
- 40
41 (115) Fischer, M. Interaction of Water with (Silico)aluminophosphate Zeotypes: A Comparative
42 Investigation Using Dispersion-Corrected DFT. *Phys. Chem. Chem. Phys.* **2016**, *18*, 15738–
43 15750.
- 44
45 (116) Bougeard, D.; Smirnov, K. S. Modelling Studies of Water in Crystalline Nanoporous
46 Aluminosilicates. *Phys. Chem. Chem. Phys.* **2007**, *9*, 226–245.
- 47
48 (117) Fois, E.; Tabacchi, G.; Quartieri, S.; Vezzalini, G. Dipolar Host/guest Interactions and
49
50
51
52
53
54
55
56
57
58
59
60

- 1
2 Geometrical Confinement at the Basis of the Stability of One-Dimensional Ice in Zeolite
3 Bikitaita. *J. Chem. Phys.* **1999**, *111*, 355–359.
- 4
5
6 (118) Alabarse, F. G.; Haines, J.; Cambon, O.; Levelut, C.; Bourgogne, D.; Haidoux, A.; Granier,
7 D.; Coasne, B. Freezing of Water Confined at the Nanoscale. *Phys. Rev. Lett.* **2012**, *109*,
8 35701.
- 9
10
11 (119) Fois, E.; Gamba, A.; Tabacchi, G.; Quartieri, S.; Vezzalini, G. Water Molecules in Single
12 File: First-Principles Studies of One-Dimensional Water Chains in Zeolites. *J. Phys. Chem. B*
13 **2001**, *105*, 3012–3016.
- 14
15
16 (120) Zhou, T.; Bai, P.; Siepmann, J. I.; Clark, A. E. Deconstructing the Confinement Effect upon
17 the Organization and Dynamics of Water in Hydrophobic Nanoporous Materials: Lessons
18 Learned from Zeolites. *J. Phys. Chem. C* **2017**, *121*, 22015–22024.
- 19
20
21 (121) Fois, E.; Gamba, A.; Tilocca, A. Structure and Dynamics of the Flexible Triple Helix of
22 Water inside VPI-5 Molecular Sieves. *J. Phys. Chem. B* **2002**, *106*, 4806–4812.
- 23
24
25 (122) Lee, Y.; Kao, C. C.; Kim, S. J.; Lee, H. H.; Lee, D. R.; Shin, T. J.; Choi, J. Y. Water
26 Nanostructures Confined inside the Quasi-One-Dimensional Channels of LTL Zeolite. *Chem.*
27 *Mater.* **2007**, *19*, 6252–6257.
- 28
29
30 (123) Trudu, F.; Tabacchi, G.; Gamba, A.; Fois, E. Water in Acid Boralites: Hydration Effects on
31 Framework B Sites. *J. Phys. Chem. C* **2008**, *112*, 15394–15401.
- 32
33
34 (124) Comboni, D.; Gatta, G. D.; Lotti, P.; Merlini, M.; Hanfland, M. Crystal-Fluid Interactions in
35 Laumontite. *Microporous Mesoporous Mater.* **2018**, *263*, 86–95.
- 36
37
38 (125) Kim, Y.; Choi, J.; Vogt, T.; Lee, Y. Structuration under Pressure: Spatial Separation of
39 Inserted Water during Pressure-Induced Hydration in Mesolite. *Am. Mineral.* **2018**, *103*,
40 175–178.
- 41
42
43 (126) Demontis, P.; Gulín-González, J.; Masia, M.; Suffritti, G. B. The Behaviour of Water
44 Confined in Zeolites: Molecular Dynamics Simulations versus Experiment. *J. Phys.*
45 *Condens. Matter* **2010**, *22*, 284106.
- 46
47
48 (127) Fois, E.; Gamba, A.; Tabacchi, G.; Quartieri, S.; Vezzalini, G. On the Collective Properties
49 of Water Molecules in One-Dimensional Zeolitic Channels. *Phys. Chem. Chem. Phys.* **2001**,
50 *3*, 4158–4163.
- 51
52
53 (128) Ceriani, C.; Fois, E.; Gamba, A.; Tabacchi, G.; Ferro, O.; Quartieri, S.; Vezzalini, G.
54 Dehydration Dynamics of Bikitaita: Part II. Ab Initio Molecular Dynamics Study. *Am.*
55 *Mineral.* **2004**, *89*, 102–109.
- 56
57
58 (129) Fischer, R. X.; Sehovic, M.; Baur, W. H.; Paulmann, C.; Gesing, T. M. Crystal Structure and
59 Morphology of Fully Hydrated Zeolite Na-A. *Zeitschrift für Krist.* **2012**, *227*, 438–445.
- 60

- 1
2
3 (130) Deiana, C.; Tabacchi, G.; Maurino, V.; Coluccia, S.; Martra, G.; Fois, E. Surface Features of
4 TiO₂ Nanoparticles: Combination Modes of Adsorbed CO Probe the Stepping of (101)
5 Facets. *Phys. Chem. Chem. Phys.* **2013**, *15*, 13391–13399.
- 6
7 (131) Coudert, F.-X.; Vuilleumier, R.; Boutin, A. Dipole Moment, Hydrogen Bonding and IR
8 Spectrum of Confined Water. *ChemPhysChem* **2006**, *7*, 2464–2467.
- 9
10 (132) Fois, E.; Gamba, A.; Tabacchi, G. Bathochromic Effects in Electronic Excitation Spectra of
11 Hydrated Ti Zeolites: A Theoretical Characterization. *ChemPhysChem* **2008**, *9*, 538–543.
- 12
13 (133) Willis, B. T. M.; Pryor, A. W. *Thermal Vibrations in Crystallography*; Cambridge University
14 Press: Cambridge, UK, 1975.
- 15
16 (134) Ruiz, A. Z.; Brühwiler, D.; Ban, T.; Calzaferri, G. Synthesis of Zeolite L. Tuning Size and
17 Morphology. *Monatshefte für Chemie* **2005**, *136*, 77–89.
- 18
19 (135) Huber, S.; Calzaferri, G. Sequential Functionalization of the Channel Entrances of Zeolite L
20 Crystals. *Angew. Chem., Int. Ed.* **2004**, *43*, 6738–6742.
- 21
22 (136) Woodtli, P.; Giger, S.; Müller, P.; Sägger, L.; Zucchetto, N.; Reber, M. J.; Ecker, A.;
23 Brühwiler, D. Indigo in the Nanochannels of Zeolite L: Towards a New Type of Colorant.
24 *Dye. Pigment.* **2018**, *149*, 456–461.
- 25
26 (137) Ramachandra, S.; Popovică, Z. D.; Schuermann, K. C.; Cucinotta, F.; Calzaferri, G.; De
27 Cola, L. Förster Resonance Energy Transfer in Quantum Dot-Dye-Loaded Zeolite L
28 Nanoassemblies. *Small* **2011**, *7*, 1488–1494.
- 29
30 (138) Huber, S.; Ruiz, A. Z.; Li, H.; Patrinoiu, G.; Botta, C.; Calzaferri, G. Optical Spectroscopy of
31 Inorganic–Organic Host–Guest Nanocrystals Organized as Oriented Monolayers. *Inorganica*
32 *Chim. Acta* **2007**, *360*, 869–875.
- 33
34 (139) Strassert, C. A.; Otter, M.; Albuquerque, R. Q.; Hone, A.; Vida, Y.; Maier, B.; De Cola, L.
35 Photoactive Hybrid Nanomaterial for Targeting, Labeling, and Killing Antibiotic-Resistant
36 Bacteria. *Angew. Chem., Int. Ed.* **2009**, *48*, 7928–7931.
- 37
38 (140) Viani, L.; Minoia, A.; Cornil, J.; Beljonne, D.; Egelhaaf, H. J.; Gierschner, J. Resonant
39 Energy Transport in Dye-Filled Monolithic Crystals of Zeolite L: Modeling of
40 Inhomogeneity. *J. Phys. Chem. C* **2016**, *120*, 27192–27199.
- 41
42 (141) Insuwan, W.; Rangsiwatananon, K.; Meeprasert, J.; Namuangruk, S.; Surakhot, Y.;
43 Kungwan, N.; Jungsuttiwong, S. Combined Experimental and Theoretical Investigation on
44 Photophysical Properties of Trans-Azobenzene Confined in LTL Zeolite: Effect of Cis-
45 Isomer Forming. *Microporous Mesoporous Mater.* **2014**, *197*, 348–357.
- 46
47
48
49
50
51
52
53
54
55
56
57
58
59
60



TOC graphics



236x221mm (72 x 72 DPI)